INFORMATION TO USERS

This material was produced from a microfilm copy of the original document. While the most advanced technological means to photograph and reproduce this document have been used, the quality is heavily dependent upon the quality of the original submitted.

The following explanation of techniques is provided to help you understand markings or patterns which may appear on this reproduction.

1. The sign or "target" for pages apparently lacking from the document photographed is "Missing Page(s)". If it was possible to obtain the missing page(s) or section, they are spliced into the film along with adjacent pages. This may have necessitated cutting thru an image and duplicating adjacent pages to insure you complete continuity.

2. When an image on the film is obliterated with a large round black mark, it is an indication that the photographer suspected that the copy may have moved during exposure and thus cause a blurred image. You will find a good image of the page in the adjacent frame.

3. When a map, drawing or chart, etc., was part of the material being photographed the photographer followed a definite method in "sectioning" the material. It is customary to begin photoing at the upper left hand corner of a large sheet and to continue photoing from left to right in equal sections with a small overlap. If necessary, sectioning is continued again — beginning below the first row and continuing on until complete.

4. The majority of users indicate that the textual content is of greatest value, however, a somewhat higher quality reproduction could be made from "photographs" if essential to the understanding of the dissertation. Silver prints of "photographs" may be ordered at additional charge by writing the Order Department, giving the catalog number, title, author and specific pages you wish reproduced.

5. PLEASE NOTE: Some pages may have indistinct print. Filmed as received.

Xerox University Microfilms
300 North Zeeb Road
Ann Arbor, Michigan 48106

75-10,301

SPLETT, John Anthony, 1946-
THE NUCLEAR STRUCTURE OF ^{159}Tb VIA
PROTON-TRANSFER REACTIONS.

The University of Michigan, Ph.D., 1974
Physics, nuclear

Xerox University Microfilms, Ann Arbor, Michigan 48106

THIS DISSERTATION HAS BEEN MICROFILMED EXACTLY AS RECEIVED.

THE NUCLEAR STRUCTURE OF ^{159}Tb VIA PROTON-TRANSFER REACTIONS

by
John Anthony Splett

A dissertation submitted in partial fulfillment
of the requirements for the degree of
Doctor of Philosophy
(Physics)
in The University of Michigan
1974

Doctoral Committee:

Professor William C. Parkinson
Associate Professor John Bardwick, III
Associate Professor Walter S. Gray
Associate Professor Henry C. Griffin
Professor Karl T. Hecht

ACKNOWLEDGEMENTS

It is a pleasure to express my gratitude to the members of my doctoral committee for their assistance throughout this project. I am particularly grateful to Professor W. C. Parkinson for his suggestions concerning the experimental aspects of this dissertation, as well as to Professors K. T. Hecht and W. S. Gray for their assistance with the theoretical and experimental aspects of the data analysis.

I am also indebted to Messrs. W. E. Downer and D. C. DuPlantis for their excellent maintenance of the cyclotron and its concomitant electrical systems, as well as to Mr. J. Koenig, who was so helpful during the long periods of data acquisition.

To the many plate-readers, who have carefully scanned the photographic emulsions used in this project, I am extremely grateful.

Finally, I wish to thank my wife for her encouragement and patience throughout my graduate study.

This work was supported in part by the United States Atomic Energy Commission.

TABLE OF CONTENTS

ACKNOWLEDGEMENTS. ii

LIST OF TABLES. iv

LIST OF ILLUSTRATIONS v

INTRODUCTION. 1

Chapter

I. THEORY. 5

A. The Nuclear Collective Model. 5
B. Nuclear Reaction Theory 27

II. EXPERIMENTAL TECHNIQUE. 37

A. The Cyclotron and Energy Analysis Systems 37
B. Limits on the Resolution Imposed by Instrumentation 38
C. Target Fabrication. 40
D. Noninstrumental Limitations on Resolution. 41
E. Particle Detection. 43
F. Determination of Differential Cross Sections. 44
G. Excitation Energies 46

III. DATA AND RESULTS. 47

A. Data. 47
B. Calculation of Coriolis Mixed Spectroscopic Strengths. 66
C. Discussion. 71

CONCLUSIONS 83

REFERENCES. 85

LIST OF TABLES

Table		Page
1.	Even-parity particle-vibrational levels in ^{159}Tb	28
2.	Optical parameters for the (^{3}He,d) reaction .	59
3.	Optical parameters for the (α,t) reaction . .	60
4.	Summary of experimental data acquired for ^{159}Tb	62
5.	Experimental energy systematics of ^{159}Tb. . .	64
6.	Comparison of experimental proton-stripping strengths	65
7.	Comparison of the experimental and theoretical spectroscopic strengths (U^2C^2) for the odd-parity states	68
8.	Comparison of the experimental and theoretical spectroscopic strengths (U^2C^2) for the even-parity states.	70

LIST OF ILLUSTRATIONS

Figure		Page
1.	Single proton levels for 50 < Z < 82	21
2.	Splitting of a shell model state under the influence of nuclear deformation	23
3.	Concepts of the pairing formalism.	26
4.	Floor plan of the experimental facility. . .	39
5.	Position spectrum for the (He,d) reaction at 10°	48
6.	Position spectrum for the (,t) reaction at 14°	49
7.	Angular distributions for the (^{3}He,d) reaction (0 to 565 keV).	52
8.	Angular distributions for the (^{3}He,d) reaction (606 to 935 keV).	53
9.	Angular distributions for the (^{3}He,d) reaction (962 to 1195 keV)	54
10.	Angular distributions for the (α,t) reaction (0 to 539 keV).	55
11.	Angular distributions for the (α,t) reaction (606 to 935 keV).	56
12.	Angular distributions for the (α,t) reaction (962 to 1088 keV)	57

INTRODUCTION

The nuclear shell model has been successful in predicting the fundamental properties of nuclei in numerous regions of the periodic table. However, it is of rather limited use in predicting the properties of nuclei with $151 \leq A \leq 180$, a region characterized by large quadrupole moments which cannot be explained on the basis of the simple spherical symmetry implied by the shell model. However, the assumption of a deformed, spheroidal potential, as implied by the unified model, leads to a comparatively simple explanation of this effect. Similarly, the collective model rather easily accounts for the rotational and vibrational spectra of these nuclei.

Although numerous β- and γ-experimental investigations have been undertaken in this region, little information beyond energy-level separations and the angular momenta of the states has been acquired. Nilsson-orbital identifications are lacking for many of the levels observed. Proton-transfer data, which expedite these determinations by means of spectroscopic "fingerprints," are lacking because of the high bombarding energies and rather stringent energy resolution requirements necessary for the success of such studies. Although the Coulomb barrier for

doubly-charged ions is ~24 MeV, standard DWBA calculations show that the angular distributions for the (α,t) and (^{3}He,d) single-proton transfer reactions in the rare-earth region remain essentially structureless until the bombarding energy reaches ~45 MeV. Gamma-ray measurements show that the average energy-level separation in this region is about 30-40 keV. Hence, a resolution of no worse than 15-20 keV is required. Previous studies in the lead region show that The University of Michigan 83-inch cyclotron, with its extensive magnetic analysis system, is capable of meeting these requirements.

Because of the availability of theoretically predicted level schemes as well as somewhat inconclusive gamma decay data for ^{159}Tb, this is a logical candidate for careful spectroscopic study. The (α,t) reaction, with its high momentum mismatch, was expected to emphasize high ℓ-transfers. It was also expected that the (^{3}He,d) reaction would act in a complementary fashion by emphasizing low ℓ-transfers. Correlation of the (α,t) data with the (^{3}He,d) results would yield experimental limits on the spectroscopic strengths, which could be compared directly with the predictions of the Nilsson plus pairing model (as modified by Soloviev). Spectroscopic information extracted from the (^{3}He,d) analysis would furnish an experimental basis for the determination of the (α,t) normalization parameter. Finally, it was hoped that both reactions would lead to

further insight into the single-proton transfer reaction mechanism in the rare-earth region.

Angular distributions for levels excited in the reactions $^{158}Gd(\alpha,t)^{159}Tb$ and $^{158}Gd(^{3}He,d)^{159}Tb$ were measured in 5° steps from 0° to 35° and 0° to 30°, respectively, at bombarding energies of E_{α} = 45.5 MeV and $E_{^{3}He}$ = 46.5 MeV. The reaction products were detected in photographic emulsions placed in the focal surface of the magnetic analysis system. Spectroscopic strengths of the levels were deduced from the measured data by comparison with DWBA-predicted distributions. The strengths were interpreted in terms of the predicted Coriolis-mixed values. The $3/2^{+}[411]$, $5/2^{+}[413]$, $5/2^{-}[532]$, $7/2^{-}[523]$, $5/2^{+}[402]$, and $7/2^{+}[404]$ bands were clearly identified. Two K = 1/2 bands with significant $1/2^{+}[411]$ single-particle strength were observed. An ℓ = 1 transition at 1068 keV was tentatively identified as the 3/2 member of the $1/2^{-}[530]$ orbital. Agreement between theoretical calculations and experimental results was found to be acceptable for all pure single-particle states, while the vibrationally admixed bands showed marked discrepancies between the experimental and Coriolis-predicted strengths.

The investigation is discussed under three major headings: theory, experimental procedure, and experimental results. Chapter I discusses the unified collective model of Bohr and Mottelson and its relation to spectroscopic

data. Chapter II describes the equipment available and modifications necessary to carry out the experiment. Finally, Chapter III summarizes the data collected and correlates them with the theory presented in Chapter I.

CHAPTER I

THEORY

A. The Nuclear Collective Model

Introduction

The nuclear rare-earth region is characterized by large quadrupole moments and, hence, spheroidal potential and density distributions. It is impossible to account for these observations on the basis of a simple pairwise occupation of the orbits of a spherical potential. An explanation lies in the assumption that the motion of the nucleons is coordinated, i.e., while the individual nucleons travel in single particle orbits, the nuclear aggregate forms an instantaneous pattern in space. If the pattern changes slowly in time compared with the single-particle variations, the motion is termed cooperative or collective. Thus, collective phenomena entail a complex interaction between particle and surface motion. If the nuclear surface is distorted, each nucleon will travel in a nonspherical potential. If the distortion is of sufficient duration, the nucleon orbits become those of an aspherical potential and thus tend to preserve the distorted shape. A closer analysis shows that the outer nu-

cleons tend to polarize the nuclear core while the latter resists and tries to maintain its sphericity. This explanation lends some insight into a mathematical description of the processes involved. Cooperative phenomena are described by collective variables to which certain portions of the total energy and angular momentum are assigned. The remaining variables describing the motion are designated internal or intrinsic. In view of the previous discussion, it may be inferred that the potential energy is minimized for the smallest surface of a given volume, i.e., the spherical case. Thus, the potential energy may be taken as quadratic in the parameters describing departures from sphericity.

The detailed summary of collective motion to be presented will follow traditional lines; the discussion will begin with an analysis of the rotational and vibrational spectra of even-even nuclei, advancing to the more complicated case of even-odd nuclear spectra.

Vibrational nuclei

Nearly spherical nuclei may be described crudely as charged quantum mechanical liquid drops. The classical analogue, subject solely to the condition of irrotational flow, was solved by Lord Rayleigh.[1] The general expression for a surface in spherical coordinates is given by

$$R = R_0 \left(1 + \sum_{\lambda\mu} \alpha_{\lambda\mu} Y_\lambda^\mu\right) \qquad \text{(A1)}$$

Let R_0 describe the surfaces of constant density. Cooperative motion is then expressed by the variation of $\alpha_{\lambda\mu}$ in time. The quadratic approximation yields kinetic and potential energies of the following form:

$$T = \frac{1}{2} \sum_{\lambda\mu} B_\lambda |\dot{\alpha}_{\lambda\mu}|^2 \tag{A2}$$

where

$$B_\lambda = \frac{\rho R_c^5}{\lambda} \tag{A3}$$

and

$$V = \frac{1}{2} \sum_{\lambda\mu} C_\lambda |\alpha_{\lambda\mu}|^2 \tag{A4}$$

where

$$C_\lambda = S R_0^2 (\lambda-1)(\lambda+2) - \frac{3}{2\pi} \frac{Z^2 e^2}{R_0} \frac{(\lambda-1)}{(2\lambda+1)} \tag{A5}$$

The B_λ are essentially order of magnitude estimates while the C_λ depend on the surface tension through S and the Coulombic repulsion through Z^2. It can be seen that the Hamiltonian of the system consists of a sum of $(2\lambda+1)$-dimensional harmonic oscillators. This result remains valid quantum mechanically and yields harmonic oscillator levels parameterized by the angular frequency ω_λ, where

$$\omega_\lambda = \left(\frac{C_\lambda}{B_\lambda}\right)^{1/2} \tag{A6}$$

It will be noted that $\omega_0 = \omega_1 = 0$. Physically, α_{00} represents a high-energy breathing mode, corresponding to nu-

clear density oscillations, while $\alpha_{1,+1}$, $\alpha_{1,-1}$, and $\alpha_{1,0}$ represent translational motion of the center of mass. Hence, the first interesting state is the $\lambda = 2$ quadrupole phonon vibration.

The general expression for excitation energy is given by

$$E = \sum_{\lambda} h_{\lambda} \hbar \omega_{\lambda} \tag{A7}$$

where h_{λ} yields the number of phonons with angular momentum quantum number λ and parity $(-1)^{\lambda}$. On the basis of this simple model, the low-lying states of an even-even nucleus are given by

1) 0^+ ground state (no phonons),
2) 2^+ first excited state at energy $h\omega_2$ (one phonon),
3) 0^+-2^+-4^+ triplet at energy $2h\omega_2$ (two phonons--symmetrically coupled, since they are bosons).

Since $\omega_3 \approx 2\omega_2$, the octupole vibration is also a possible second excited state. The vibrational model breaks down beyond the second excited state because of the increasing number of single-particle degrees of freedom.

Rotational nuclei

Vibrational nuclei are adequately described by the formalism of the previous section because the $\alpha_{\lambda\mu}$ depict the change of the nuclear shape in time with respect to

fixed axes rather accurately. In the rotational case, the $\alpha_{\lambda\mu}$ change in time but the nuclear shape remains constant. Therefore, it is reasonable to expect to describe the system in terms of the nuclear orientation in space and a pertinent set of deformation parameters. The orientation of the nucleus is given by the Euler angles of the body-fixed axes with respect to the space-fixed axes. Let us represent the $\alpha_{\lambda\mu}$ in the body-fixed system by a_μ. Since the products of inertia vanish in the principal axes system, $a_{2,\pm1} = 0$ and $a_{2,2} = a_{2,-2}$. Next we define

$$a_0 = \beta \cos\gamma \tag{A8}$$

and

$$a_2 = \frac{\beta}{\sqrt{2}} \sin\gamma \tag{A9}$$

where β is a measure of the total deformation of the nucleus, and γ is a measure of the deviation of the nuclear shape from axial symmetry. Utilizing the fact that $\alpha^*_{\lambda\mu}$ transforms like γ^μ_λ under rotations, we may write (A2) in the following form:

$$T = \frac{1}{2} B(\dot\beta^2 + \beta^2\dot\gamma^2) + \frac{1}{2}\sum_{K=1}^{3} \mathcal{I}_K \omega_K^2 \tag{A10}$$

where

$$\mathcal{I}_K = 4B\beta^2 \sin^2(\gamma - \tfrac{2\pi}{3}K) \tag{A11}$$

and each of the ω_K represents a component of the angular velocity of the body-fixed axes with respect to the space-

fixed axes. When $\gamma = 0$ or π,

$$\vartheta_3 = 0$$

$$\vartheta_1 = \vartheta_2 = \vartheta_0 = 3B\beta^2$$

and the system is axially symmetric. The irrotational flow model yields the following expression for ϑ_0:

$$\vartheta_0 = \left(\frac{45}{16\pi}\right)\beta^2 \vartheta_{rig} \qquad 2$$

where ϑ_{rig} is the moment of inertia of a sphere about its diameter. Since β^2 is small, only a small fraction of the rigid sphere inertia contributes to collective motion. Thus, a rotation may be visualized as a wave of nuclear matter traveling along the nuclear surface. Also, since the spherical nuclei, with their complete symmetry with respect to the three nuclear axes, show no rotational states, it may be inferred that the nuclear moment of inertia about an axis of symmetry vanishes. Hence, ϑ_3 is indeed negligible for axially symmetric nuclei.

The next step in the analysis requires a quantization of the Hamiltonian of the system. This may be effected by expressing the velocities in (A10) in terms of their conjugate momenta and, subsequently, rewriting the latter in terms of differential operators. The result is the following quantum mechanical Hamiltonian:

$$H = H_\beta + H_\gamma + \sum_{K=1}^{3} \frac{L_K^2}{2\vartheta_K} + \frac{1}{2} C\beta^2 \qquad \text{(A12)}$$

where H_β and H_γ are essentially harmonic oscillator equations in β and γ, respectively, and L_κ is an angular momentum operator about the k-axis (body-fixed). As Landau and Lifschitz[3] point out, the L_κ satisfy the commutation relation $[L_i,L_j] = -iL_\kappa$, since they refer to a set of moving axes. Since $[H,\vec{L}^2] = 0$ and $[H,L_Z] = 0$, $\vec{L}^2$ and L_Z are constants of motion. If the 3-axis (body-fixed) is an axis of symmetry, $[H,L_3] = 0$. Thus, we have the following constants of motion and their respective eigenvalues:

1) $\vec{L}^2$: $I(I+1)$

2) L_Z : M

3) L_3 : K .

The eigenfunctions are given by the standard D^I_{MK}. While the wave functions are single-valued in $\alpha_{2\mu}$, it is found that 24 classes of body-fixed axes correspond to the same $\alpha_{2\mu}$. Hence, the wave function must be invariant under changes of body-fixed axes which do not alter the $\alpha_{2\mu}$. These changes may be compounded from the following operations: rotations of 180° about the 1-axis, rotations of 90° about the 3-axis, and cyclic permutation of body-fixed axes. The appropriate wave functions are given by

$$|IMK;\lambda,\nu\rangle = f^{(\delta)}_{\delta,K,\lambda,\nu}\, g_K^{I,\lambda(\gamma)} \left[\frac{2I+1}{16\pi^2(1+\delta_{K0})}\right]^{1/2} \left\{D^I_{MK} + (-1)^I D^I_{M,-K}\right\} \quad \text{(A13)}$$

where λ and ν are quantum numbers associated with the β- and γ-vibrations; the energies are given by

$$E = E_\beta + E_\gamma + \frac{\hbar^2}{2\mathcal{I}_0} I(I+1) \qquad \text{(A14)}$$

Physically, the energies correspond to rotational bands based on β- and γ-vibrational states. The wave functions indicate that I must be even for K = 0 or I $\geq$ K otherwise; β-excitations correspond to preservation of axial symmetry but variation in deformation; they are characterized by K = 0 and lie above ~1 MeV in excitation. Gamma-vibrations correspond to an axial asymmetry and are characterized by K = 2; they begin to appear at ~0.5 MeV.

The discussion of rotational nuclei marks the end of our description of even-even nuclei. The results apply to odd-even nuclei, provided that single-particle effects are properly included.

Single-particle excitations

As we have seen, there is a rather intimate relationship between the shape of the nucleus and the paths of the individual nucleons comprising the latter. Much of our discussion has relied on the assumption that the nuclear deformation was small. In general, the collective potential energy is minimized for β = 0. However, for certain N and Z the energy of the individual orbits minimizes for $\beta \neq 0$, $\gamma \neq 0$. Hence, the equilibrium shape of the nucleus becomes aspherical. The particle and collective motions are then said to be strongly coupled.

Under these conditions the system may be described by the quantum mechanical Hamiltonian

$$H = H_c + H_p \tag{A15}$$

where H_c is the collective contribution depending on β, γ, and the Euler angles, and H_p is the single particle term, which, in the case of odd-even rare-earth nuclei, describes the single nucleon traveling outside the even-even core. In this approximation β and γ appear in H_p as parameters. This assumption is valid provided that the change in shape is slow compared with the spatial variation of the individual nucleons. This is called the adiabatic approximation.

The single-particle problem reduces to a search for solutions of the equation

$$H_p \psi_\alpha = E_\alpha(\beta,\gamma)\psi_\alpha \tag{A16}$$

where β and γ are parameters determined such that the total particle energy is minimized. Let us rewrite H_p as

$$H_p = T + V(\beta,\gamma,\vec{r},\vec{\ell},\vec{s}). \tag{A17}$$

If we assume that the equipotentials follow the surfaces of constant density, we may write

$$V(\beta,\gamma,\vec{r},\vec{\ell},\vec{s}) = V_0(\beta,\gamma,R_0,\vec{\ell},\vec{s})$$

$$= V_0\left(\beta,\gamma,\frac{R}{1+\sum_\mu a_\mu Y_2^\mu},\vec{\ell},\vec{s}\right). \tag{A18}$$

Further, we absorb $\frac{1}{2}C\beta^2$ into H_p since this maneuver traces the surface energy to the interparticle energy. Thus, the

rotational kinetic energy T_{rot} is set equal to H_c. The Schrödinger equation for the complete system becomes

$$(T_{rot}+H_p)\Psi = E\Psi \tag{A19}$$

where

$$T_{rot} = \sum_{K=1}^{3} \frac{R_K^2}{2\vartheta_K}$$

$$= \sum_{K=1}^{3} \frac{(I_K - j_K)^2}{2\vartheta_K} \tag{A20}$$

with $\vec{I}$ representing the total nuclear angular momentum and $\vec{j}$ the single-particle angular momentum. Physically, $\vec{R}$ represents the angular momentum imparted by the nucleus to the system to make $\vec{I}$ a constant of the motion. In the axially symmetric case,

$$T_{rot} = \frac{\hbar^2}{2\vartheta_0}\left[(\vec{I}-\vec{j})^2-(I_3-j_3)^2\right] + \frac{\hbar^2}{2\vartheta_3}(I_3-j_3)^2 \tag{A21}$$

Since $V(\beta,\gamma,\vec{r},\vec{\ell},\vec{s})$ is axially symmetric, the azimuthal angles do not appear in H_p and j_3 becomes a constant of the motion. Direct calculation shows that $[T_{rot},\vec{I}^2] = 0$ and $[T_{rot}, I_3] = 0$. Letting Ω represent the eigenvalue of j_3 and expanding (A21), we find

$$T_{rot} = \frac{\hbar^2}{2\vartheta_0}\left[I(I+1)-K^2-\Omega^2\right] + \frac{\hbar^2}{2\vartheta_3}(K-\Omega)^2$$

$$-\frac{\hbar^2}{2\vartheta_0}(I_+ j_- + I_- j_+) + \frac{\hbar^2}{2\vartheta_0}\vec{j}^2. \tag{A22}$$

(In the axially symmetric case $\vartheta_3 = 0$ and, thus, $K = \Omega$.

Hence, $\vec{R}$ is perpendicular to the symmetry axis.) The term in $\vec{j}^2$ is absorbed into H_p, and the second term on the right is called the Coriolis term in analogy with the classical Coriolis energy $\frac{1}{2}\vec{\omega}\cdot\vec{L}$. (Hereafter, this term shall be called H_{RPC}.) If the single-particle energies are widely separated, H_{RPC} may be neglected. When this is not valid, H_{RPC} must be diagonalized. This requires a knowledge of the wave function for the complete system. Ignoring H_{RPC}, we find from (A19) that

$$\Psi(IMK\Omega) \sim \chi_\Omega D^I_{MK}$$

where χ_Ω is a single-particle wave function. Since $V(\beta,\gamma,\vec{r},\vec{\ell},\vec{s})$ is not spherically symmetric, $\vec{j}^2$ is not a constant of the motion. Thus, we may write

$$\chi_\Omega = \sum_j C_{j\Omega}\chi_{j\Omega} \qquad \text{(A23)}$$

where $\chi_{j\Omega}$ is an eigenfunction of a spherically symmetric potential. An analysis of the effect of a 180° rotation about the 1-axis on χ_Ω and D^I_{MK} leads to the following expression for the normalized wave function for the entire system:

$$\Psi(IMK\Omega) = \left(\frac{2I+1}{16\pi^2}\right)^{1/2}\left\{\chi_\Omega D^I_{MK} + (-1)^{I+\Omega}\chi_{-\Omega} D^I_{M,-K}\right\} \qquad \text{(A24)}$$

(with $K = \Omega$). An analysis of H_{RPC} shows that it may connect only states differing by a unit change in K. Thus, the only nonvanishing diagonal term of H_{RPC} occurs for $K = 1/2$. Here,

$$\langle IMK\Omega | H_{RPC} | IMK\Omega \rangle = \frac{\hbar^2}{2\mathcal{I}_0} a (-1)^{I+1/2} (I+1/2) \tag{A25}$$

with

$$a = -\sum_j (-1)^{j+1/2} (j+1/2) |C_{j\frac{1}{2}}|^2 ; \tag{A26}$$

a is called the decoupling parameter, the value of which determines the level ordering in a K = 1/2 band. In the event that nearly degenerate single-particle energies differing by unit K exist in the region of interest, $\langle IMK+1\Omega+1|H_{RPC}|IMK\Omega\rangle$ must be evaluated and the resultant matrix diagonalized. The eigenfunctions will be linear combinations of the pertinent $\overline{\Psi}(IMK\Omega)$.

To summarize, we may write the energy expression for an odd-even rotational band as

$$E_{I,K} = E_K + \frac{\hbar^2}{2\mathcal{I}_0} [I(I+1) - 2K^2 + \delta_{K,1/2} a (-1)^{I+1/2} (I+1/2)] \tag{A27}$$

where E_K is a single-particle energy and $I \geq K$. The energies increase with increasing I for $K \neq 1/2$.

Having considered the rotational spectrum of the odd-even nuclei, we turn to the final problem of our discussion, the description of the single-particle spectrum. The solution we shall discuss is that originally formulated by Nilsson. The problem reduces to a solution of the equation

$$H_p \overline{\Psi}_\alpha = E_\alpha(\beta,\gamma) \overline{\Psi}_\alpha$$

or

$$\left[-\frac{\hbar^2}{2M}\nabla^2 + V_0\left(\beta,\gamma;\frac{R}{1+\sum_\mu \alpha_\mu Y_2^\mu},\vec{l},\vec{s}\right)\right]\Psi_\alpha = E_\alpha(\beta,\gamma)\,\Psi_\alpha,$$

where M is the mass of the nucleon. If we allow for the possibility of a momentum-dependent potential, M must be replaced by the effective mass μ^* which is ~0.5-0.7M. The equation to be solved then becomes

$$\left[-\frac{\hbar^2}{2\mu^*}\nabla^2 + V_0'\left(\beta,\gamma;\frac{R}{1+\sum_\mu \alpha_\mu Y_2^\mu},\vec{l},\vec{s}\right)\right]\Psi_\alpha = E_\alpha(\beta,\gamma)\,\Psi_\alpha \tag{A28}$$

where V_0' is momentum-independent;

$$V_0'\left(\beta,\gamma;\frac{R}{1+\sum_\mu \alpha_\mu Y_2^\mu},\vec{l},\vec{s}\right)$$

must reproduce the observed level structure for spherical nuclei when $\beta = 0$. Hence, it must be a well intermediate between a harmonic oscillator and a square; a spin-orbit term is required to give the proper level ordering. Nilsson[4] performed his calculation with a harmonic oscillator of the form $\underline{K}(R_0)^2$ or

$$V_0'\left(\beta,\gamma;\frac{R}{f},\vec{l},\vec{s}\right) = \underline{K}\left(\frac{R}{f}\right)^2 \tag{A29}$$

where

$$f = 1 + \sum_\mu \alpha_\mu Y_2^\mu$$

$$= 1 + \beta(\cos\gamma)Y_2^0 + \frac{\beta}{\sqrt{2}}(\sin\gamma)\left(Y_2^2 + Y_2^{-2}\right) \tag{A30}$$

To first order in β, this is equivalent to

$$\underline{K}\left(\frac{x_1^2}{A_1^2} + \frac{x_2^2}{A_2^2} + \frac{x_3^2}{A_3^2}\right)$$

with

$$A_K = 1 + \sqrt{\frac{5}{4\pi}}\,\beta \cos\left(\gamma - \frac{2}{3}\pi K\right) \tag{A31}$$

Thus, the equipotentials are ellipsoids with axes in the same ratio as the surfaces of constant density. We note that $A_1A_2A_3 = 1$ (to first order): this implies that the nuclear volume is constant. If we let

$$\omega_K^2 = 2\bar{K}/\mu^* A_K^2 \tag{A32}$$

and

$$V_h = \tfrac{1}{2}\mu^* \sum_{K=1}^{3} \omega_K^2 x_K^2 \tag{A33}$$

equation (A28) becomes

$$\left(-\frac{\hbar^2}{2\mu^*}\nabla^2 + V_h + V_{\vec{\ell},\vec{s}}\right)\psi_\alpha = E_\alpha \psi_\alpha \tag{A34}$$

where $V_{\vec{\ell},\vec{s}}$ is the spin-orbit coupling term. We further simplify by letting

$$\xi_K = \left(\frac{\mu^* \omega_K}{\hbar}\right)^{1/2} x_K \tag{A35}$$

Then

$$H_h = -\frac{\hbar^2}{2\mu^*}\nabla^2 + V_h = \sum_K \tfrac{1}{2}\hbar\omega_K \left(-\frac{\partial^2}{\partial \xi_K^2} + \xi_K^2\right). \tag{A36}$$

As a final simplification, we define

$$\rho^2 = \sum_K \xi_K^2, \tag{A37}$$

$$\nabla_\xi^2 = \sum_K \frac{\partial^2}{\partial \xi_K^2} \tag{A38}$$

$$\omega_0 = \frac{2E}{\mu^*}, \tag{A39}$$

$$\omega_K = \omega_0 (1+\delta_K). \tag{A40}$$

Then,

$$H_h = H_0 + H_E \tag{A41}$$

where

$$H_0 = \frac{1}{2}\hbar\omega_0 (-\nabla_\xi^2 + \rho^2), \tag{A42}$$

$$H_E = \frac{1}{2}\hbar\omega_0 \sum_K \delta_K \left(-\frac{\partial^2}{\partial\xi_K^2} + \xi_K^2\right). \tag{A43}$$

Nilsson further defined a pseudo-orbital angular momentum

$$\vec{\lambda} = \frac{\hbar}{i}\vec{\xi}\times\vec{\nabla}_\xi. \tag{A44}$$

Noting that $[H_0,\vec{\lambda}^2] = 0$ and $[H_0,\lambda_3] = 0$, he attributed the eigenvalues $\ell(\ell+1)$ and Λ to $\vec{\lambda}^2$ and λ_3, respectively; the eigenstates were labeled $|N\ell\Lambda\Sigma\rangle$, where N is the principal (harmonic oscillator) quantum number and Σ is the spin projection along the 3-axis. In this formalism $V_{\vec{\ell},\vec{s}}$ was given simply by $C\vec{\lambda}\cdot\vec{\Sigma}$. An additional term of the form $D\vec{\lambda}^2$ was added to depress the high angular momentum states from their harmonic oscillator values. Thus, (A34) became

$$(H_0 + H_E + C\vec{\lambda}\cdot\vec{\Sigma} + D\vec{\lambda}^2)\psi_\alpha = E_\alpha\psi_\alpha \tag{A45}$$

with eigenfunctions

$$\chi_\Omega = \sum_{\ell,\Lambda} a_{\ell\Lambda\Omega}\,|N\ell\Lambda\Sigma\rangle \tag{A46}$$

(Variations in N were not allowed since (A43) may connect states in which N differs by 2: this was thought to corre-

spond to a large energy difference.) δ_K was defined so that

$$\delta_1 = \delta_2 = \frac{\delta}{3}, \tag{A47}$$

$$\delta_3 = -\frac{2}{3}\delta \tag{A48}$$

where

$$\delta = \left(\frac{15}{8\pi}\right)^{1/2}\beta \qquad \text{(correct to first order only)} \tag{A49}$$

The $a_{\ell\Lambda\Omega}$ were determined by numerical diagonalization of (A45). C was chosen to yield the spherical level ordering; D was adjusted from shell to shell; $\hbar\omega_o \sim 41/A^{1/3}$ MeV (with a mild δ dependence). The $a_{\ell\Lambda\Omega}$ were tabulated along with their energies, and plots were made of energy versus deformation for various regions of the periodic table. Figure 1 illustrates the plot for the rare-earth region. The levels are labeled by the expressions $\Omega^{\pi}[Nn_3\Lambda]$, where N, n_3, and Λ are determined by the component of the wave function which remains as $\delta \to \infty$. (n_3 is the number of oscillator quanta along the 3-axis.)

The eigenfunctions may be written in terms of a spherical basis $\chi_{j\Omega}$ if we choose

$$c^{j}_{\ell\Lambda\Omega} = \sum_{\Lambda} \langle \ell\, \Lambda\, \tfrac{1}{2}\, \Sigma | j\, \Omega \rangle\, a_{\ell\Lambda\Omega}.$$

In this case the selection rules require $\Omega \leq j \leq N+1/2$. This approach indicates that the deformation destroys the degeneracy of the shell model states. Each spherical state separates into (2j+1)/2 states. (The 1/2 results from time-

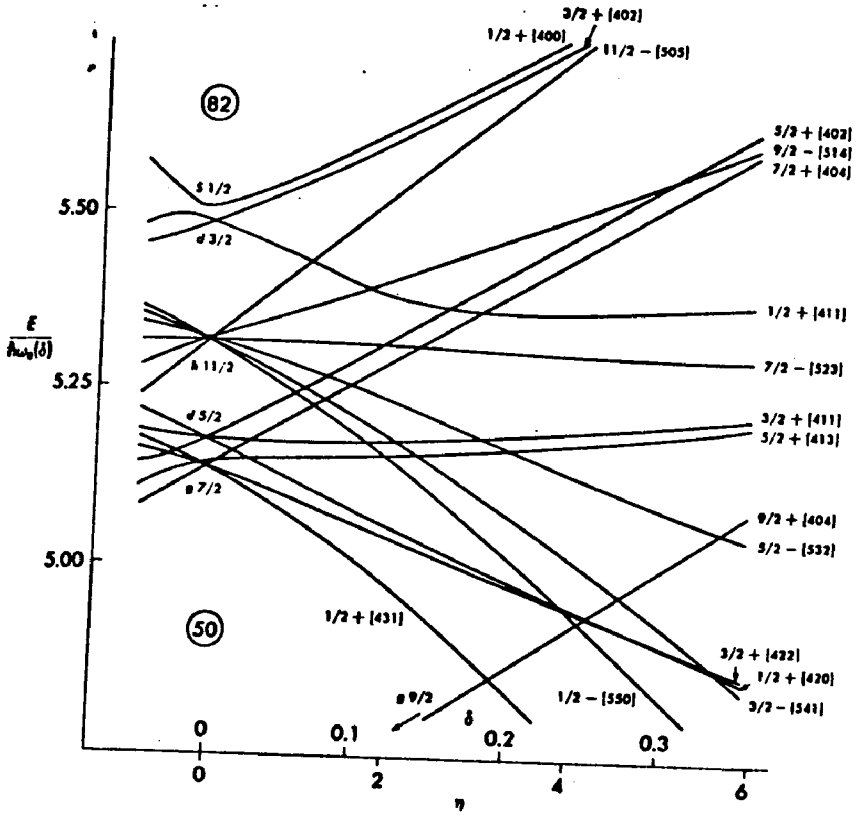


Fig. 1.--Single proton levels for $50 < Z < 82$.[4]

reversal invariance.) The ordering of the states may be determined from the fact that $\omega_3 < \omega_1$ for $\delta > 0$. For large Ω the particle spends much time in the plane perpendicular to the 3-axis. Hence, its energy must be high. For small Ω the particle spends more time parallel to the 3-axis. Thus, its energy is small. Figure 2 illustrates these concepts.

At this point it is prudent to note that modern investigators believe that introduction of a pseudo-orbital angular momentum is an unnecessary complication. With realistic spin and orbital angular momenta, the Nilsson Hamiltonian (A45) is normally written

$$(H_0 + H_E - 2K\vec{\ell}\cdot\vec{s} - \mu K\vec{\ell}^2)\psi_\alpha = E_\alpha \psi_\alpha \qquad \text{(A50)}$$

The accuracy of the extreme single-particle Nilsson model is, at best, rather crude. Attempts to embellish the model with more elaborate potential wells and higher order deformation parameters have not fully accounted for the observed spectra. Pairing corrections must be included.

Pairing theory

The short-range attractive nature of the nucleon-nucleon interaction causes nucleons to adopt configurations which produce maximum spatial overlap. However, the Pauli principle prevents more than one nucleon from occupying the same state. Since the two-nucleon interaction commutes with the time-reversal operator,

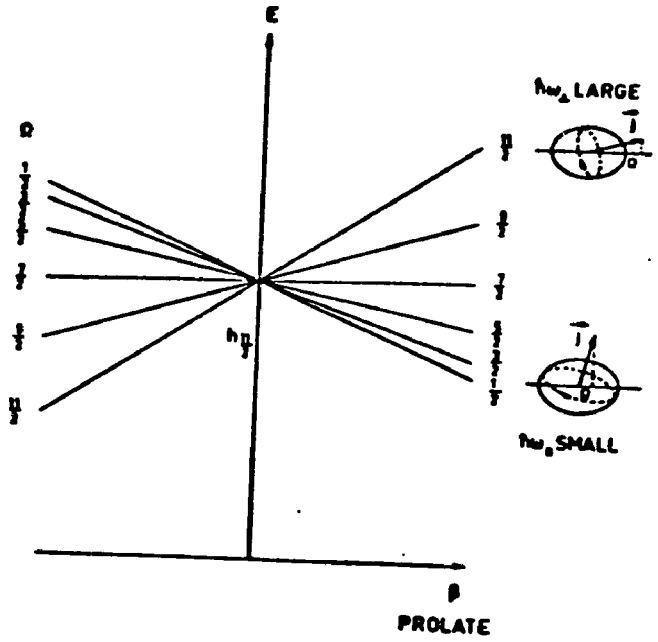


Fig. 2.--Splitting of a shell model state under the influence of nuclear deformation. The 2j+1 fold degenerate spherical state is split into (2j+1)/2 doubly degenerate deformed states. The ordering of the states with the high Ω-values highest for prolate deformation, is preserved in the general Nilsson model.[5]

a state and its time-reversed partner are degenerate. These wave functions have a large overlap since their only physical difference lies in the sign of their projection (Ω) quantum number. Hence, the deepest lying nuclear states are characterized by a pairwise filling of the Ω-degenerate orbits. It is impossible to state with certainty whether a level near the Fermi level is occupied. A BCS approach expresses this uncertainty by defining the parameters V_α^2 and U_α^2, where V_α^2 denotes the probability that a level is occupied by a pair, and U_α^2 designates the probability that a level is emptied. (We note $U_\alpha^2 + V_\alpha^2 = 1$.) In even-odd nuclei V_α^2 indicates the extent to which a state behaves like a hole, and U_α^2 indicates the extent to which a state is a particle (relative to the even-even nucleus). Such a state, with both particle and hole characteristics, is called a quasiparticle. The (observed) energy spectrum is given by the difference between excited- and ground-state-quasiparticle energies:

$$E_\nu - E_{G.S.} \approx \sqrt{(\xi_\nu - \lambda)^2 + \Delta^2} - \sqrt{(\xi_{G.S.} - \lambda)^2 + \Delta^2} \approx E_\nu - \Delta \qquad \text{(A51)}$$

where ξ_ν and $\xi_{G.S.}$ are single-particle energies, λ is the Fermi level, and Δ is 1/2 the energy gap between the ground- and first-excited states of the neighboring even-even nucleus. Δ is also a measure of the diffuseness of the Fermi surface since

$$V_\alpha^2 = \frac{1}{2}\left(1 - \frac{\xi_\alpha - \lambda}{\sqrt{(\xi_\alpha - \lambda)^2 + \Delta^2}}\right) \tag{A52}$$

Physically, the inclusion of pairing effects tends to compress the energy spectrum and force many levels into the region of the ground state. Higher levels are depressed by ~Δ. These effects are illustrated in Figure 3.

Collective phenomena

Soloviev[6] has attempted a more complete discussion of the even-odd problem by considering a quasiparticle Hamiltonian, which includes pairing- and multipole-multipole effects. (Pairing accounts for the tendency of the nucleus to assume a spherical configuration while multipole interactions describe the opposing tendency toward deformation.) The solutions assume the following comparatively simple form:

$$\psi(K^\pi) = \Omega(K^\pi)\,\underline{\Psi}_0 \tag{A53}$$

With

$$\Omega(K^\pi) = \frac{C_\rho}{\sqrt{2}}\left\{\sum_\sigma \alpha^+_{\rho\sigma} + \sum_{\substack{\lambda\mu i \\ \rho\mu\sigma}} D^{\lambda\mu i}_{\rho\nu}\,\alpha^+_{\nu\sigma}\,Q^+_i(\lambda\mu)\right\} \tag{A54}$$

where $\underline{\Psi}_0$ is the quasi-particle vacuum, $\alpha^+_{\rho\sigma}$ is a quasi-particle in state ρ with time-reversal characters, and $Q^+_i(\lambda\mu)$ creates a phonon of character $(\lambda\mu)$. ($Q^+_i(\lambda\mu)$ is a linear combination of two-quasi-particle states.) Physically, $\psi(K^\pi)$ tells us the relative single-particle and

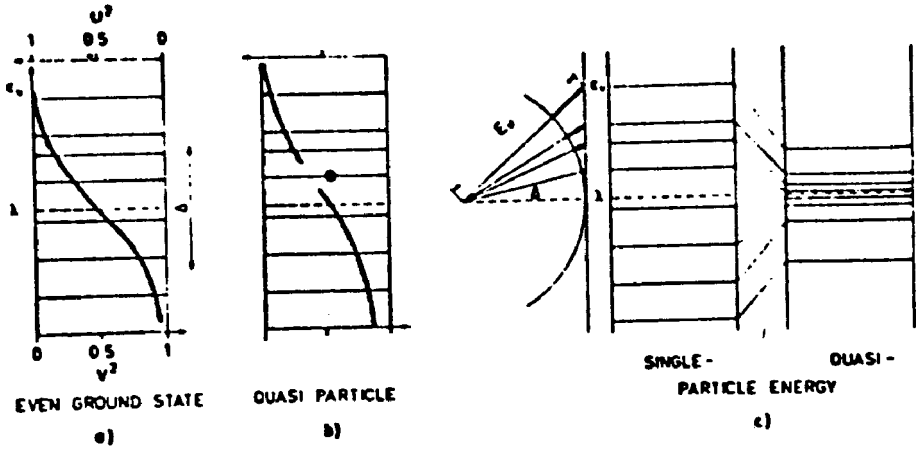


Fig. 3.--Concepts of the pairing formalism. (a) The occupation by pairs of the single particle levels near the Fermi surface is measured by the U^2 and V^2 factors. (b) An odd particle causes rearrangement in the distribution shown in (a). It is thus a "quasiparticle." (c) The geometrical construction to the left gives the quasiparticle energies. The E_ν is the hypotenuse in the right-angle triangle with sides Δ and $\epsilon_\nu - \lambda$. The Δ is approximately equal to the quasiparticle energy of the ground state. When Δ is subtracted from the E_ν's, the differences (the black arrows) are the quasiparticle energies relative to the ground state which are shown to the right.[5]

particle-collective strengths in a given state. In macroscopic terms $Q_i^+(22)$ designates a gamma vibration (γ), while $Q_i^+(20)$ designates a beta vibration (β). The results of such a calculation for ^{159}Tb are given in Table 1. The energies quoted are experimental, while the state admixtures are those given by the Soloviev[6] calculations.

Having completed our discussion of nuclear models, we now attempt to relate it to physically measurable elements through reaction theory.

B. Nuclear Reaction Theory

Stripping and pickup for shell-model nuclei

Stripping and pickup are special types of direct reaction. Satchler[7] has characterized direct reactions in the following manner: if there exists a strong overlap between incident and exit channels so that a collision may occur with little rearrangement, the reaction will occur quickly and is said to be direct. Direct reactions are further described by scattering amplitudes, which vary smoothly with energy; their angular distributions show a marked dependence on the orbital angular momentum of the particle(s) transferred.

Since direct reaction theory is rather intricate and, in addition, has been discussed in detail elsewhere, only a brief outline of the techniques involved in calculating a (^{3}He,d) differential cross section will be pre-

TABLE 1

EVEN-PARITY PARTICLE-VIBRATIONAL LEVELS IN ^{159}Tb

K	Energy (keV)	Structure
$3/2^+$	0	$(3/2^+[411])90\%$; $(1/2^+[411] + \gamma)8\%$
$5/2^+$	348	$(5/2^+[413])94\%$; $(1/2^+[411] + \gamma)4\%$
$1/2^+$	580	$(1/2^+[411])60\%$; $(3/2^+[411] + \gamma)30\%$
$1/2^+$	971	$(5/2^+[413] + \gamma)80\%$; $(3/2^+[411] + \gamma)15\%$

sented here. (The (d,^{3}He) cross section may be obtained by time-reversal invariance; the (α,t) cross section is formally identical to the (^{3}He,d) cross section since both are stripping reactions.) Symbolically, a (^{3}He,d) reaction may be represented by

$$T + {}^3He \rightarrow F + d$$

where T and F represent the target and residual nuclei, respectively. Three basic assumptions will be made regarding the physics of this reaction:

1) The projectile (^{3}He) travels in an average field due to the target represented by the optical potential.
2) The transferred proton enters a single-particle orbital in the target, i.e., the core remains unchanged.
3) The emitted particle (d) is affected by the residual nucleus through purely elastic mechanisms.

In the DWBA (Distorted Wave Born Approximation) representation the Hamiltonian of the system in the initial state is represented by

$$H = H_{^3He} + H_T + T_{^3He} + V_{^3He}^{OPT} = H_i^\circ \qquad \text{(B1)}$$

where $H_{^3He}$ and H_T describe the internal motions of the ^{3}He and the target, respectively; $T_{^3He}$ represents the kinetic

energy of ^{3}He with respect to the target; V_{He}^{OPT} is the complex optical potential. Similarly, in the final state we expect

$$H = H_F + H_d + T_d + V_{dF} \tag{B2}$$

If we assume that most of the d-F interaction is included in V_d^{OPT}, $V_{dF} \approx V_{dp} + V_d^{OPT}$ and

$$H = H_f^\circ + V_{dp} \tag{B3}$$

Formal scattering theory tells us that we may calculate the differential cross section from

$$\frac{d\sigma}{d\Omega} = \frac{\mu_i \mu_f}{(2\pi\hbar^2)^2} \left(\frac{K_f}{K_i}\right) \Sigma |S_{fi}|^2 \tag{B4}$$

where μ_i and μ_f are the reduced masses in the entrance and exit channels, respectively; K_i and K_f are the initial and final relative wave vectors; S_{fi} denotes the transition amplitude; Σ designates an average over initial states and sum over final states. (All geometric factors have been suppressed.) The transition amplitude is given by

$$S_{fi} = \langle \phi_f(K_f) | V_{dp} | \Psi_i(K_i) \rangle \tag{B5}$$

where

$$H_f^\circ \phi_f(\vec{K_f}) = \left(E_d + E_F + \frac{\hbar^2 \vec{K_f}^2}{2\mu_f}\right) \phi_f(\vec{K_f}) \tag{B6}$$

and

$$H\Psi_i(\vec{K}_i) = E\Psi_i(\vec{K}_i) \tag{B7}$$

(E_d and E_F are the pertinent internal energies; E is the total energy of the system.) The first-order Born approximation yields

$$\phi_i(\vec{K}_i) \approx \Psi_i(\vec{K}_i) \tag{B8}$$

where

$$H_i^0\phi_i(\vec{K}_i) = \left(E_{^3He} + E_T + \frac{\hbar^2\vec{K}_i^2}{2\mu_i}\right)\phi_i(\vec{K}_i) \tag{B9}$$

($E_{^3He}$ and E_T are once again internal energies.) Under these circumstances

$$\phi_i(\vec{K}_i) = \chi_{^3He}\chi_T\,\psi_i(\vec{K}_i) \tag{B10}$$

where $\chi_{^3He}$ and χ_T are internal wave-functions; $\psi_i(\vec{K}_i)$ describes the motion of the ^{3}He in the target field and is called a "distorted" wave. Similarly,

$$\phi_f(\vec{K}_f) = \chi_d\chi_F\,\psi_f(\vec{K}_f) \tag{B11}.$$

Thus,

$$S_{fi} = \int \psi_f^*(\vec{K}_f)\chi_d^*\chi_F^*\,V_{dp}\,\chi_{^3He}\,\chi_T\,\psi_i(\vec{K}_i)\,d\vec{r}_{^3He}\,d\vec{r}_T\,d\vec{r}_d\,d\vec{r}_F \tag{B12}.$$

Next, we expand χ_F in terms of basis states represented by the product of a single-proton wave function and a core wave function:

$$\chi_F = \sum_{\ell_j}\alpha_{N\ell_j}\,\phi_{N\ell_j}\,\chi_{F'} \tag{B13},$$

where $\phi_{N\ell j}$ is the single-particle wave function. Finally,

we make the approximation that the d is created where the ^{3}He vanishes (zero-range approximation), i.e.,

$$\chi_d^* V_{dp} \chi_{^3He} \approx D_0 \, \delta(\vec{r}_p - \vec{r}_d) \qquad \text{(B14)}.$$

The result becomes

$$S_{fi} = D_0 \sum_{\ell j} \alpha^*_{N\ell j} \int \chi_T \chi_F \, d\tau_N \; \psi_i(\vec{K}_i) \, \phi^*_{N\ell j} \, \psi^*_f(\vec{K}_f) \, d\tau \qquad \text{(B15)}.$$

This enables us to write the differential cross section in the following simple form:

$$\frac{d\sigma}{d\Omega_{(^3He,d)}} = \frac{(2I_f+1)}{(2I_i+1)} N^{(+)} \sum_{j\ell} \sigma_\ell^{(+)} S_{j\ell}^{(+)} \qquad \text{(B16)}.$$

("+" denotes stripping.) By the principle of time-reversal invariance,

$$\frac{d\sigma}{d\Omega_{(d,^3He)}} = N^{(-)} \sum_{j\ell} \sigma_\ell^{(-)} S_{j\ell}^{(-)} \qquad \text{(B17)}.$$

For ease in discussion of N, $S_{j\ell}$, and σ_ℓ, we consider reactions with an even-even target. Here,

$$\frac{d\sigma}{d\Omega_{(^3He,d)}} = (2j+1) N^{(+)} \sigma_\ell^{(+)} S_{j\ell}^{(+)} \qquad \text{(B18)}$$

and

$$\frac{d\sigma}{d\Omega_{(d,^3He)}} = N^{(-)} \sigma_\ell^{(-)} S_{j\ell}^{(-)} \qquad \text{(B19)}.$$

Let us now describe the physical meaning of the parameters N, $S_{j\ell}$, and σ_ℓ:

1) N is a normalization constant depending on D_0. Hence, it is a measure of the overlap between the ^{3}He and the d internal states. It is usu-

ally determined by the use of the Hulthén and Irving-Gunn wave functions. We note that N must be available before $S_{j\ell}$ can be determined.

2) $S_{j\ell}$ is proportional to $|\alpha^{*}_{N\ell j}\int\chi_T\chi_{F'}d\tau|^2$. It is called the spectroscopic factor and contains all of the nuclear structure information. Briefly, it tells us how much the residual nucleus looks like the target plus a single particle. If a single proton is added to a closed shell, $S^{(+)}_{j\ell} = \alpha^2_{N\ell j}$; if $\chi_{F'} = \chi_T$, $S^{(+)}_{j\ell} = 1$. If a shell-model level contains n nucleons, $S^{(+)}_{j\ell}$ is spread over many levels, but

$$\Sigma S^{(+)}_{j\ell} = \frac{(2j+1)-n}{(2j+1)} \qquad \text{(B20)}$$

Thus, $S^{(+)}_{j\ell}$ may be interpreted as the emptiness probability U^2. Similarly,

$$\Sigma S^{(-)}_{j\ell} = n \qquad \text{(B21)}$$

and

$$V^2 = \frac{\Sigma S^{(-)}_{j\ell}}{(2j+1)} \qquad \text{(B22)}$$

Hence, the total stripping and pickup cross sections for a given (ℓ,j) are given by

$$\frac{d\sigma}{d\Omega\,(^3He,d)} = (2j+1)N^{(+)}\sigma^{(+)}_{\ell}U^2 \qquad \text{(B23)}$$

and

$$\frac{d\sigma}{d\Omega_{(d,^3He)}} = (2j+1)\, N^{(-)} \sigma_\ell^{(-)}\, V^2 \qquad \text{(B24)}.$$

3) σ_ℓ is proportional to $\left|\int \psi_o^{-}(\vec{K}_i)\, \Phi^*_{N\ell j}\, \psi_f^*(\vec{K}_f)\, d\tau\right|^2$ and depends on nuclear structure solely through $\Phi_{N\ell j}$. Hence, it contains essentially no structure information but is totally responsible for the shape of the angular distribution. σ_ℓ is the function that is usually calculated by DWBA codes.

Now, it remains to adapt the conclusions of the present section to the case of deformed nuclei.

Single-proton transfer reactions on deformed nuclei

An analysis of the physical content of (B23) and (B24) offers some insight into the expressions for proton-transfer cross sections in the rare-earth region. For convenience we repeat (B23) and (B24):

$$\frac{d\sigma}{d\Omega_{(^3He,d)}} = (2j+1)\, N^{(+)} \sigma_\ell^{(+)}\, U^2,$$

$$\frac{d\sigma}{d\Omega_{(d,^3He)}} = (2j+1)\, N^{(-)} \sigma_\ell^{(-)}\, V^2.$$

We note that (2j+1) indicates the number of states available for population by stripping and pickup while U^2 and V^2 represent the usual emptiness and fullness parameters. In the rare-earth region the Nilsson scheme offers two levels for population ($\pm\Omega$) while each Nilsson state contains a $C^2_{j\ell}$ contribution from the (ℓ,j) shell model state.

(We use the more descriptive $C^2_{j\ell}$ for $C^2_{j\Omega}$.) Hence, in the rare-earth region

$$\frac{d\sigma}{d\Omega(^3He,d)} = \frac{2C^2_{j\ell}}{2j+1} N^{(+)}\sigma_\ell^{(+)} U^2 \qquad \text{(B25)}$$

and

$$\frac{d\sigma}{d\Omega(d,^3He)} = 2C^2_{j\ell} N^{(-)}\sigma_\ell^{(-)} V^2 \qquad \text{(B26)}.$$

These equations show that single-proton transfer reactions display the spherical components of the Nilsson wave functions via $C^2_{j\ell}$. Physically, each j transfer depicts a member of the rotational band built on the Ω single-particle state; for this band member the total angular momentum is given by j. This may be seen from an analysis of the pickup reaction. If a nucleon of angular momentum j is extracted from an even-even target, the residual nucleus is left in a state of angular momentum j. Since j is not a good quantum number for a particle in a deformed well, the nucleus must furnish a rotational angular momentum $\vec{R}$ to make the total angular momentum $(\vec{R}+\vec{j})$ a constant of the motion. Hence, the intimate relationship between single-proton transfer states and rotational spectra is revealed.

It should be noted that (B25) and (B26) apply to purely single-particle spectra. If we introduce the Soloviev complication, we expect (B25) and (B26) to be reduced by a factor of C^2_ρ, where the latter represents the single-particle contribution to the nuclear wave func-

tion. If Coriolis coupling is to be included, Tjøm and Elbek[5] show that the cross sections become

$$\frac{d\sigma}{d\Omega_{(^3He,d)}} = \frac{1}{(2j+1)}\left(\sum_h U_n a_n C^n_{\ell j}\right)^2 N^{(+)}\sigma_\ell^{(+)} \qquad \text{(B27)}$$

and

$$\frac{d\sigma}{d\Omega_{(d,^3He)}} = 2\left(\sum_h V_n a_n C^n_{\ell j}\right)^2 N^{(-)}\sigma_\ell^{(-)} \qquad \text{(B28)}$$

where the a_n are the amplitudes of the Nilsson contributions to the Coriolis-corrected wave function.

To summarize, we believe that comparison of (^{3}He,d) data with (B25) will enable us to calculate $(\Sigma_n U_n a_n C^n_{\ell j})^2$ (or $(\Sigma_n U_n a_n C^n_{\ell j} C^{(n)}_\rho)^2$) for the ^{159}Tb spectrum. Comparison of these results with (α,t) data will provide a normalization for the (α,t) reaction. Departures from predicted angular distributions will offer insight into the reaction mechanisms which are operative.

CHAPTER II

EXPERIMENTAL TECHNIQUE

A. The Cyclotron and Energy Analysis Systems

The University of Michigan 83-inch sector-focused, isochronous cyclotron facility is capable of accelerating alpha particles in the 22-80 MeV region and ^{3}He ions in the 22-100 MeV range and providing beams of particles to the target with an ion optical resolving power $E/\Delta E = 8 \times 10^3$. As discussed in the introduction, nuclear structure considerations suggested the use of 45 MeV alpha particle and ^{3}He ion beams. In addition, the close spacing of the levels imposes stringent requirements on the instrumental resolution. A description of the instrumentation and its resolution capabilities has been treated in detail elsewhere;[9] hence, only a brief summary is given here. The beam preparation system, consisting of two 110°, 2 meter radius, double-focusing, n = 1/2 magnets, was used to provide beams to the target with a coherent energy spread of less than 30 keV and with a full convergence angle of 0.8°. The reaction products analysis system consists of three double-focusing, 1.33 meter radius, n ≈ 1/2 magnets, which are dispersion-matched with the beam prepa-

ration system. However, because dispersion cancellation depends on the kinematics of the reaction and the properties of the target, it was necessary to use only two of the three analyzer magnets. Figure 4 is a floor plan of the cyclotron and analyzer vaults.

B. Limits on the Resolution Imposed by Instrumentation

Although one might naively expect the instrumentation routinely to provide a resolution of 8×10^3, this is seldom achieved in an actual measurement. The discrepancy can be attributed in part to the instrument and in part to kinematic effects. Kinematic effects, which are a function of the target, are discussed in a later section. Instrumental limitations which pertain directly to the cyclotron are: the effective source-width, the brightness and stability of the beam, and source-incoherence. Brightness affects the beam current of a given energy spread. Stability is a function of the regulation of the various cyclotron components. The effective source-width and coherence depends on the quality of the tune. A nominal effective source-width of 0.5 mm contributes a minimum of 6 keV/mm $\times$ 0.5 mm = 3 keV to the energy spread at an incident energy of 45 MeV. A coherent source is characterized by the emitted particles having energies which vary monotonically from one edge of the source to the other. An incoherent source, on the other hand, emits particles of all energies

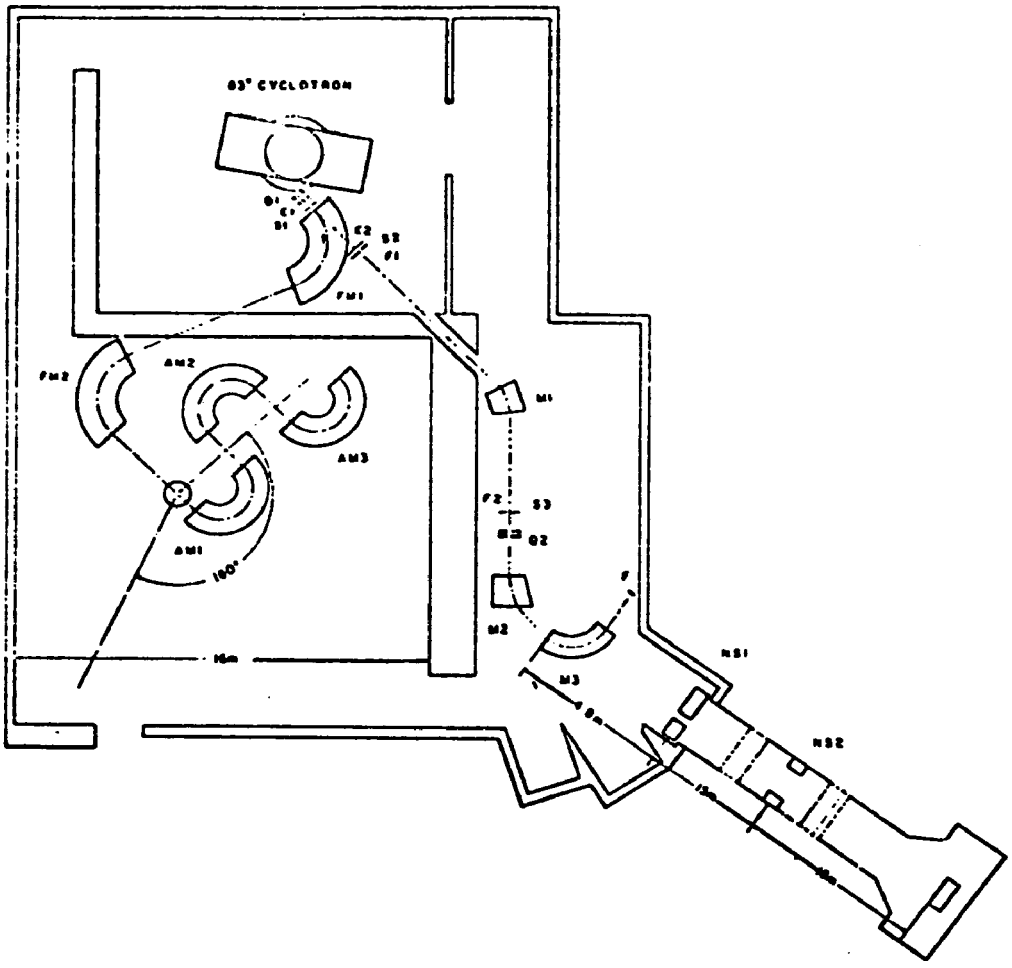


Fig. 4.--Floor plan of the experimental facility.

Source: W. C. Parkinson, J. F. Petersen, Robert H. Day, D. C. DuPlantis, W. S. Gray, and John Bardwick, Nucl. Inst. and Meth., 119, 61 (1974).

extracted from the cyclotron from each element of the source. If the source is coherent, the energy spread is independent of source-width and may be cancelled by the analyzer magnets. Incoherent effects may never be cancelled. A more complete discussion of cyclotron-related effects is presented by Parkinson and Bardwick.[9]

Stability of the field in the magnetic systems is monitored and regulated by means of NMR probes. A drift in the frequency of the probes is directly related to the incident and outgoing particle momenta and becomes a measure of the energy uncertainty in the spectroscopic experiments. Measurement of the maximum allowable frequency drift implied a variation of ≤ 1 keV in the energies of the outgoing particles.

C. Target Fabrication

Gadolinium targets were initially produced by direct evaporation of enriched ^{158}Gd metal from a molybdenum boat onto 20 $\mu g/cm^2$ Yissum[10] carbon foils. This process yielded a thin (~5 $\mu g/cm^2$) target which was not used for extensive measurements because of the excessive exposure times required--~16 hours for ~300 counts under a one mb/sr peak with a 300 nA alpha particle beam. To produce thicker targets by this method, a higher power input was required but the resulting thermal radiation either destroyed the carbon backing or rendered it so hot that

condensation could not take place. The problem was solved by the construction of a 2-kilowatt electron gun, which would focus ~2 keV electrons on an enriched ^{158}Gd oxide pellet of 1/8 inch diameter. In this way, a high but local power density could be obtained. Using this technique, targets of up to 100 $\mu g/cm^2$ thickness were fabricated with an efficiency of 1 $\mu g/cm^2$ per mg of isotope used.

D. Noninstrumental Limitations on Resolution

Given a high quality ion-optical system, the energy resolution obtained in a given experiment is nearly always determined by the properties of the target. For a given target thickness the resolution can be significantly improved by a judicious choice of target angle. Three factors influence the choice of target angle:[11] beam spot width, target thickness, and straggling. For a coherent beam the geometric width of the image at the focal surface of the magnetic analysis system is given by

$$\Delta y = S\left[\frac{\cos(\theta-\alpha)}{\cos\alpha} - \frac{2}{3}\frac{E_1}{E_2}\frac{dE_2}{dE_1}\right] \qquad \text{(D1)}$$

where θ is the scattering angle, α is the angle between the normal to the plane of the target and the incident beam direction, S is the width of the illuminated area of the target, and E_1 and E_2 are the incident and outgoing particle energies, respectively. For large S (a necessity for thin targets) the resolution is significantly degraded

unless the target angle α is adjusted to minimize the quantity in brackets.

The finite thickness of the target induces an energy spread because the nuclear reaction may occur anywhere in the volume determined by the beam spot and target thickness. The energy spread is given by

$$\Delta E_t = t\left[\left(\frac{dE}{dx_1}\right)\frac{1}{\cos\alpha} - \left(\frac{dE}{dx}\right)_2 \frac{1}{\cos(\theta-\alpha)}\right] \qquad \text{(D2)}$$

where t is the target thickness, and the subscripts (1) and (2) refer to the incident and outgoing particles, respectively.

Straggling refers to the energy spread induced by interactions with atomic electrons. By analogy with the derivation of (D2), it was shown that the RMS energy spread due to straggling is given by

$$\Delta E_{ST} = 18\sqrt{t}\left(\frac{Z_1}{\cos\alpha} + \frac{Z_2}{\cos(\theta-\alpha)}\right)^{1/2} \qquad \text{(D3)}$$

where t is given in mg/cm^2, ΔE_{ST} is given in keV, and Z_1 and Z_2 refer to the atomic numbers of the incident and outgoing particles, respectively.

For large source widths ($S \geq 4$ mm) Δy would account for the bulk of the energy spread ($\geq$24 keV) if the source were incoherent and dispersion cancellation were not used. The energy uncertainties due to straggling and target thickness, ΔE_{ST} and ΔE_t, respectively, when added in quadrature for a 50 $\mu g/cm^2$ Gd_2O_3 target with a 20 $\mu g/cm^2$ carbon backing, yield no greater than an 18 keV spread. Hence, the target angle was chosen to effect complete beam spot

cancellation and the FWHM was predicted to be no greater than 18 keV. For small slit widths ($\leq$1 mm) it was found that all three effects became significant. Concurrent minimization of the effects led to 15-keV resolution.

E. Particle Detection

The reaction products of the (α,t) and $(^3He,d)$ reactions were recorded in Ilford K2 photographic emulsions. Wedge-shaped aluminum absorbers were placed directly in front of the emulsions to maximize the ionization density in the latter. A byproduct of the use of the absorbers was the elimination of doubly-charged ions which might enter the emulsions. The emulsions were located at a position with respect to the magnetic focal surface to minimize the image width resulting from the kinematic broadening term $\left|\frac{\partial E_2}{\partial \theta}\right|$.

The data were corrected for any variation in target thickness with time and the uncertainty in the target angle measurement by monitoring the incident particles elastically scattered by the target. The monitor counter was a phosphorous-diffused solid state detector. In addition, at small angles where the geometry precluded the use of the Faraday cup, the elastic-scattering monitor count rate was used as a measure of the beam intensity.

For scattering angles $\leq 10°$ the reaction products emanating from collisions between the incident beam and

the walls of the analyzer magnet duct can produce an extremely high background count. Since the helium ions have a lower magnetic rigidity than the singly-charged rare-earth reaction products, it is possible to minimize the background by offsetting the slits, which define the solid angle, relative to the optic axis. This procedure stops the helium ions at a point in the magnet such that the production of singly-charged background reaction products is minimized.

F. Determination of Differential Cross Sections

The differential scattering cross section, which is essentially a normalized reaction yield, is given by

$$\frac{d\sigma}{d\Omega} = \frac{\Delta N_o}{N_i N \Delta\Omega} \qquad \text{(F1)}$$

where ΔN_o is the number of particles detected, N is the number of particles per cm^2 presented to the beam, and $\Delta\Omega$ is the solid angle of the detector. The number of nuclei N seen by the incident beam is given by

$$N = \frac{6.023 \times 10^{20} t}{A \cos\alpha} \qquad \text{(F2)}$$

where t is the target thickness in mg/cm^2, A is the atomic mass of the target, and α is the target angle. Thus,

$$\frac{d\sigma}{d\Omega} = \frac{2.66 \times 10^{-4} Q (\cos\alpha) \Delta N_o}{\Delta\Omega \, t \, Q_i} \; mb/sr \qquad \text{(F3)}$$

where Q is the charge of the incident particle in electron

units, and Q_i is the impinging charge in nanocoulombs. Hence, the primary sources of error in the determination of the differential cross section are ΔN_o, t, Q_i, and $\Delta\Omega$. When nuclear emulsions are used for particle detection, ΔN_o is subject to plate-reading errors and to statistical uncertainty. The emulsions used in the (α,t) measurements were usually scanned in half-millimeter swaths at one-millimeter intervals, while for the $(^3He,d)$ reaction, because of the lower intensities, the scanning was done in half-millimeter swaths at half-millimeter intervals. Plate re-reading and comparison of peak-shape throughout the angular distributions indicated the reading error was no greater than 10%. The statistical uncertainty in the number of counts in a peak is $\sim 1/\sqrt{N}$ in the large-number Poisson approximation, which holds down to $N \approx 100$. Since the number of counts under any given peak was infrequently less than 100, the uncertainty in ΔN_o was less than 14%, since the plate-reading error and statistical uncertainty are independent. Uncertainties in t and Q_i were eliminated by normalization to the elastic scattering peak. The monitor data are subject to a 3% error due to statistical uncertainty and target angle and solid angle errors. The spectrometer solid angle was determined to within an accuracy of 10% from data previously measured at this laboratory.[12] Hence, the total uncertainty in $\frac{d\sigma}{d\Omega}$ was estimated to be 15%. (Use of the peak-fitting program AUTOFIT showed that peak-fitting er-

rors could cause the total error to increase to about 25%.)

The beam energy was monitored by an NMR probe mounted in the second beam preparation magnet, which was previously calibrated using the 14.233 MeV proton elastic resonance on ^{12}C.[13] The incident particle energies were determined to be 45.5 MeV for the alpha particles and 46.5 MeV for the ^{3}He ions.

G. Excitation Energies

Excitation energies were determined using the following geometrical formula:[12]

$$E(x) = \frac{2E_0 x \cos\gamma}{B + A(d_0 + x\sin\gamma)} + E_0 \qquad \text{(G1)}$$

where E(x) is the particle energy in MeV, E_0 is the optic axis energy, d_0 is the image distance in cm, γ is the tilt of the focal plane, and x is the distance from the optic axis in cm. (E(x) increases with x; B = 634.213 and A = 4.59.) The excitation energies predicted by (G1) were compared with the energies cited in gamma decay studies. The comparison showed that the excitation energies deduced from (G1) were accurate to within 15 keV.

CHAPTER III

DATA AND RESULTS

A. Data

Angular distributions for the $^{158}Gd(^{3}He,d)^{159}Tb$ and $^{158}Gd(\alpha,t)^{159}Tb$ reactions were measured from 0° to 30° and 0° to 35°, respectively, in 5° steps. Representative ($^{3}He,d$) and (α,t) spectra are displayed in Figures 5 and 6. The respective ground state Q-values for the ($^{3}He,d$) and (α,t) reactions are 0.702 MeV and -13.618 MeV (UCRL-16964). The 15-keV resolution in the ($^{3}He,d$) spectrum at 10° is typical of the resolution observed in that reaction. Levels 3 and 4 are tentatively identified because they are characterized by high ℓ-transfers and low Nilsson coefficients. These states are clearly visible in the (α,t) spectrum. The presence of a copper impurity between them in the ($^{3}He,d$) measurement at 10° further hinders their identification. The peak between levels 15 and 16 is attributable to a copper impurity which moves out of the spectrum beyond 20°. The (α,t) spectrum at 17°, for which the resolution is 20 keV, represents a special measurement using a 2° spectrometer acceptance angle performed to optimize resolution. It can be seen that most of the levels de-

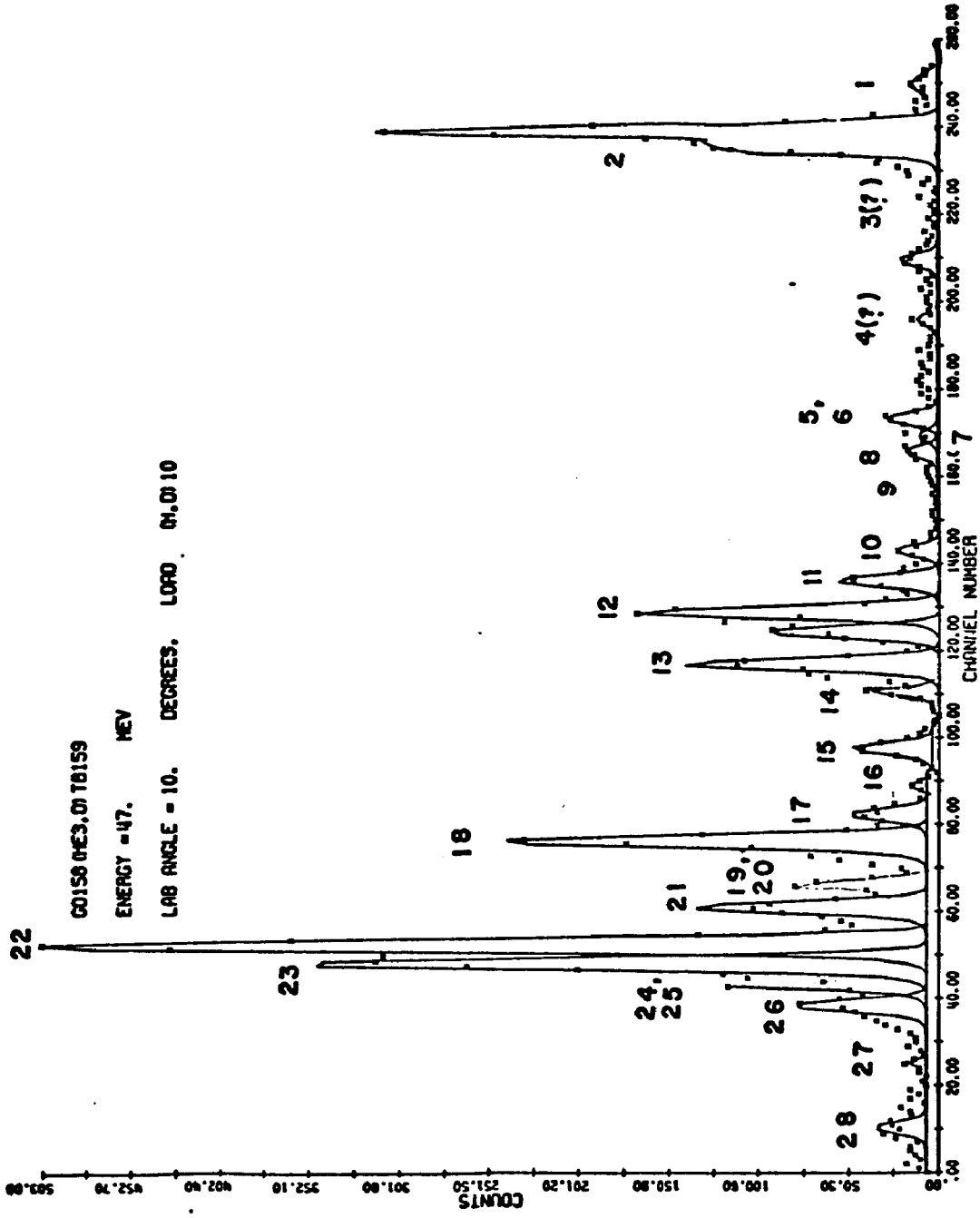


Fig. 5.--Position spectrum for the (^{3}He,d) reaction at 10°.

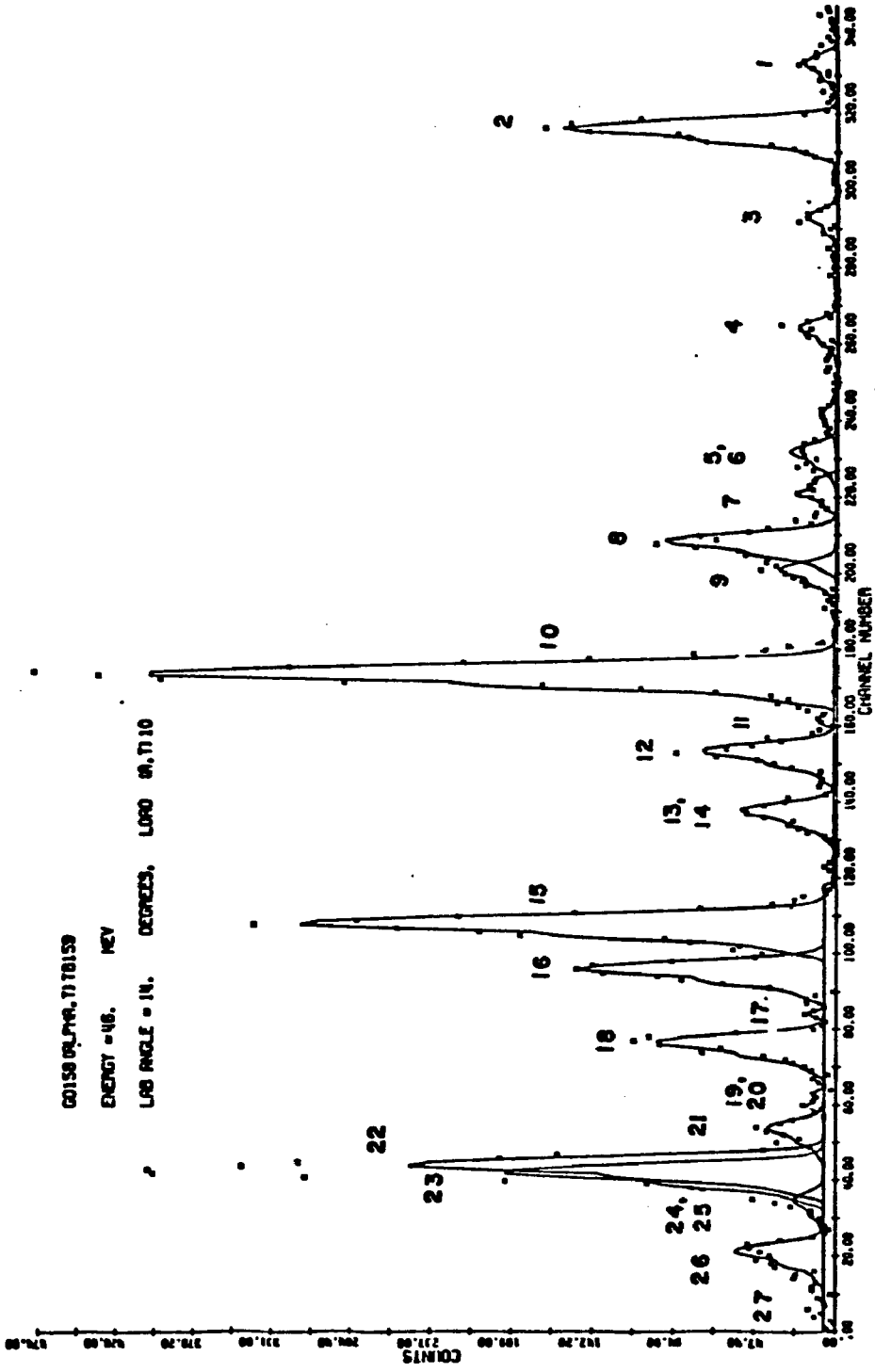


Fig. 6.--Position spectrum for the (α,t) reaction at 14°.

tected in the (^{3}He,d) measurement are present in the spectrum. A more typical resolution for the (α,t) reaction was ~25 keV, and as a result, the weakly excited states labeled "10" and "15" are obscured.

The many overlapping peaks between 500 and 1200 keV were disentangled by the use of the computer program AUTOFIT.[14] Because of the high dispersion (5 keV/mm) and good resolution in the (^{3}He,d) measurement, the levels were easily disentangled by the use of the "standard-peak" option available in the program. This option, however, neglects the small tails on the peaks due to straggling, but these were shown to be no more than a 5% effect. The lower dispersion (3.6 keV/mm) and poorer resolution of the (α,t) experiment required the use of observed line shapes of isolated peaks in the spectrum, such as level "2," for the analysis. Hence, tail contributions were not neglected. Thus, the spectroscopic strengths extracted from the (α,t) measurement are expected to be larger than those deduced from the (^{3}He,d) analysis.

Reaction cross sections were calculated using formula (F3) described in the previous chapter. The target thicknesses were calculated from the elastic scattering peaks measured by the monitor counter at 30° and 35° for the (^{3}He,d) and (α,t) studies, respectively. A different target was used for each of the two angular distributions because of the finite lifetime of thin gadolinium targets.

The elastic scattering measurements of Broad and Lewis[15] showed that use of the DWBA-predicted elastic cross section for normalization calculations in this angular region is reasonable, provided that it is realized that the DWBA calculation yields a reasonable estimate of the 0^+-ground state and the first 2^+-excited state cross sections. Because of the small energy separation between these levels in the rare-earth region (~100 keV), the monitor counter is unable to resolve the two states and, hence, measures the combined cross section of the two levels. For the two targets used, the target thicknesses were calculated to be 98 $\mu g/cm^2$ and 92 $\mu g/cm^2$ for the (α,t) and $(^3He,d)$ reactions, respectively. (The uncertainty of $\leq 1°$ in the monitor angle resulted in a 5% uncertainty in the elastic cross section.) Previous measurements at this laboratory[15] indicated that the solid angle of the spectrometer is 0.65 ± 0.07 msr for an acceptance angle of 4° (when two analysis magnets are employed). The differential cross sections were plotted in the CM frame of reference, although kinematical calculations indicated that CM angles and cross sections differed little from their LAB counterparts. The width of the beam spot on the target introduced an angular spread in scattering angle of no greater that 0.2°, which is adequately represented by the width of the dots representing the data points. (The 4° acceptance angle was taken into account by the DWBA averaging process.)

The measured $(^3He,d)$ angular distributions are shown in Figures 7, 8, and 9, while Figures 10, 11, and 12

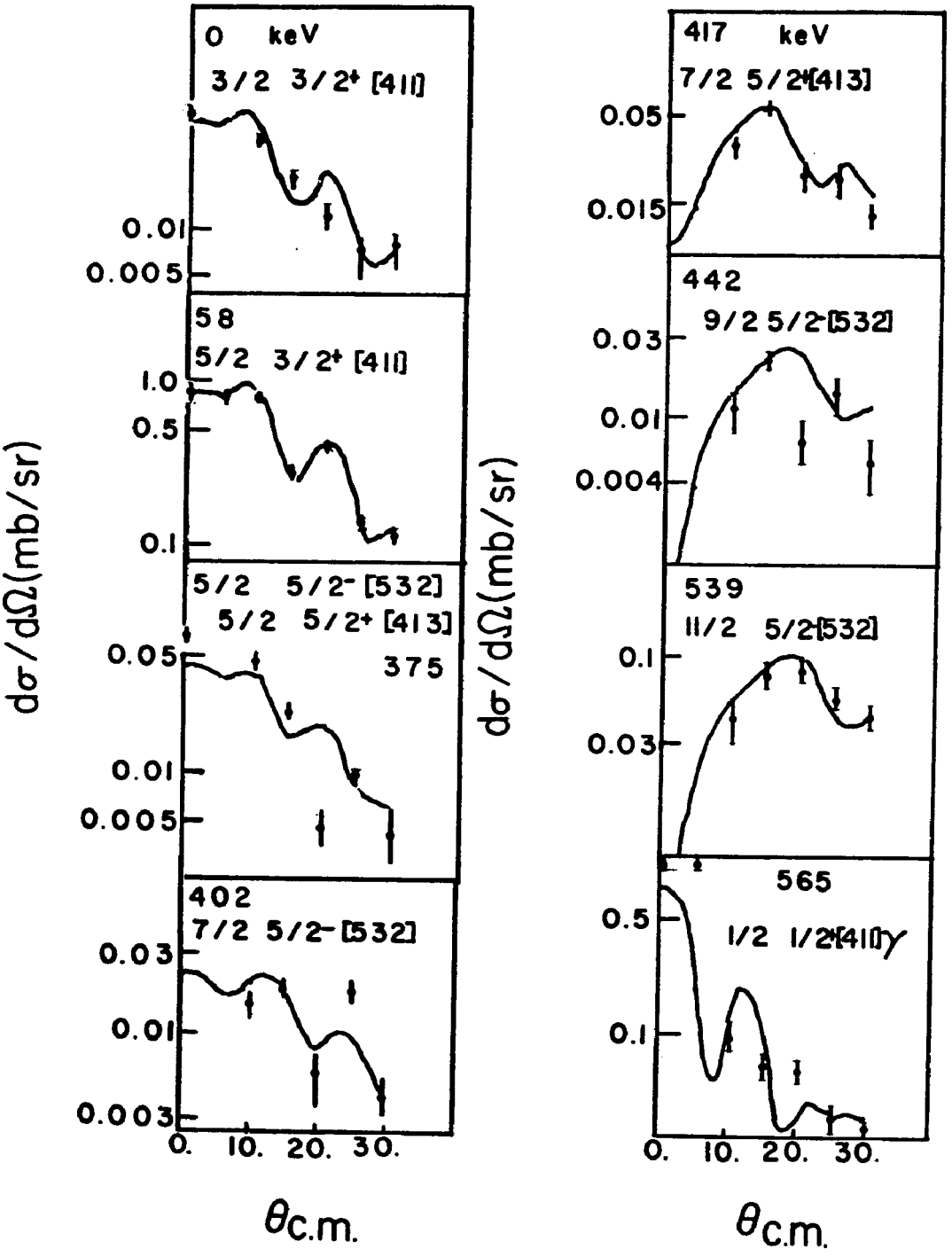


Fig. 7.--Angular distributions for the (^{3}He,d) reaction (0 to 565 keV).

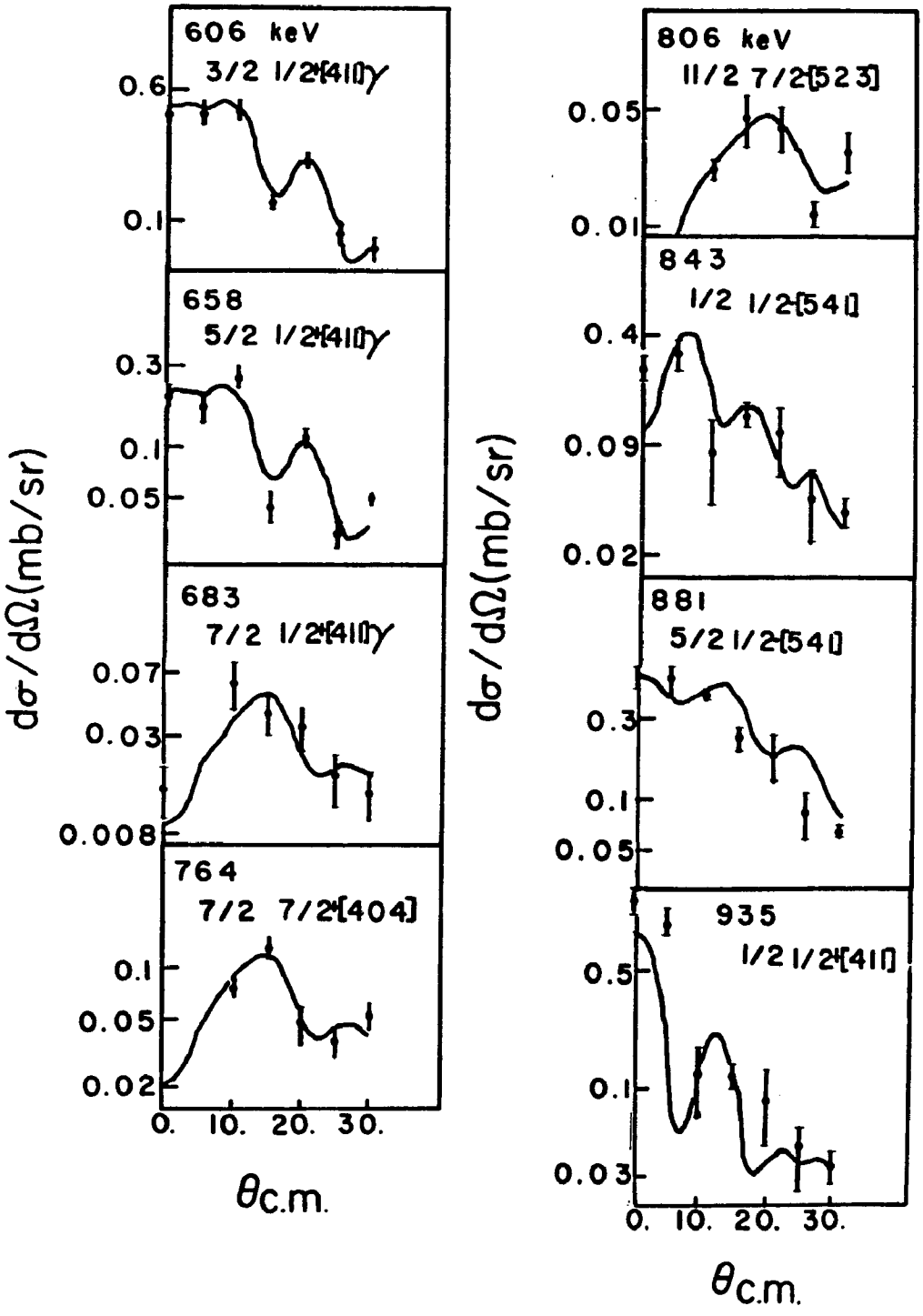


Fig. 8.--Angular distributions for the (^{3}He,d) reaction (606 to 935 keV).

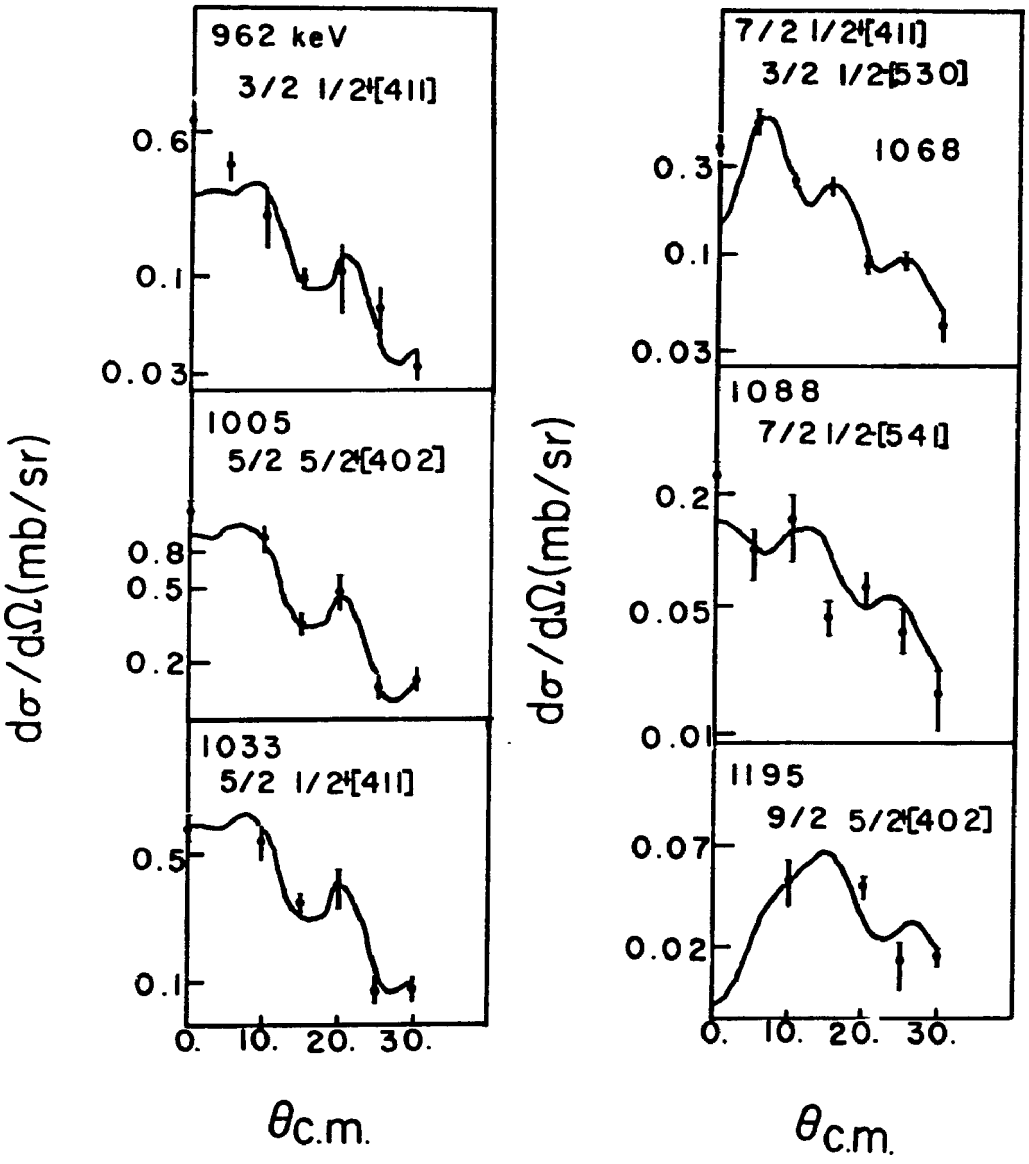


Fig. 9.--Angular distributions for the (^{3}He,d) reaction (962 to 1195 keV).

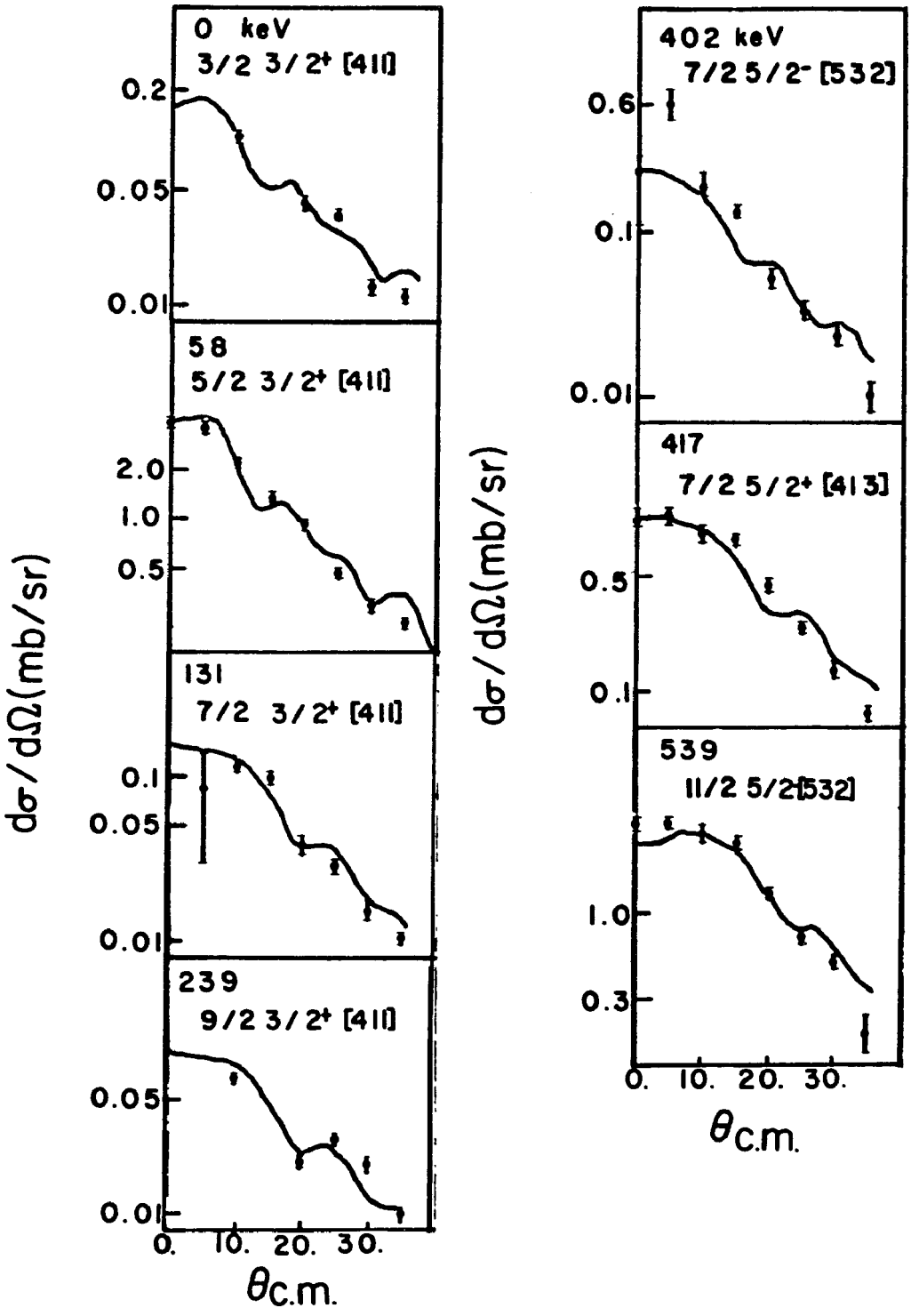


Fig. 10.--Angular distributions for the (α,t) reaction (0 to 539 keV).

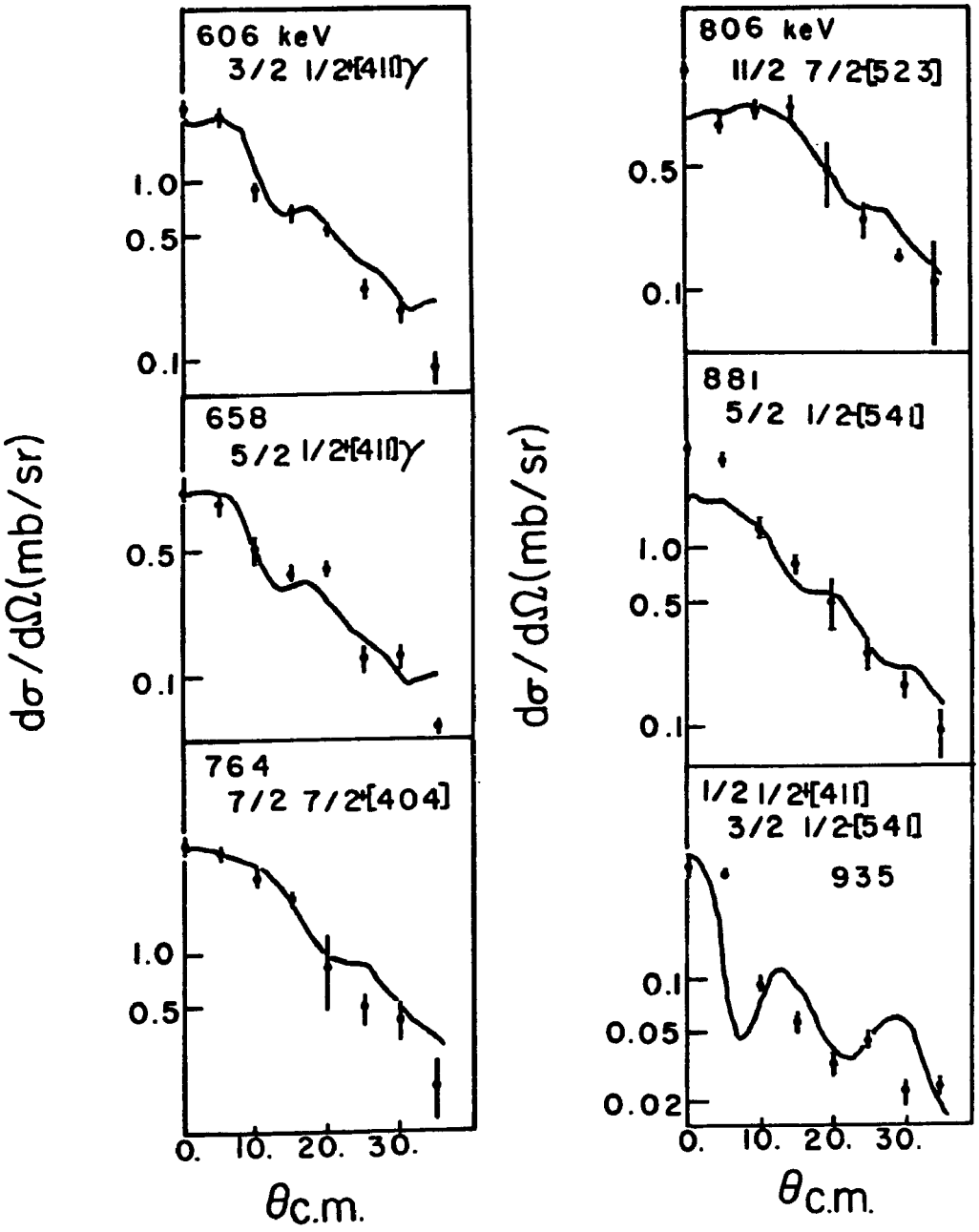


Fig. 11.--Angular distributions for the (α,t) reaction (606 to 935 keV).

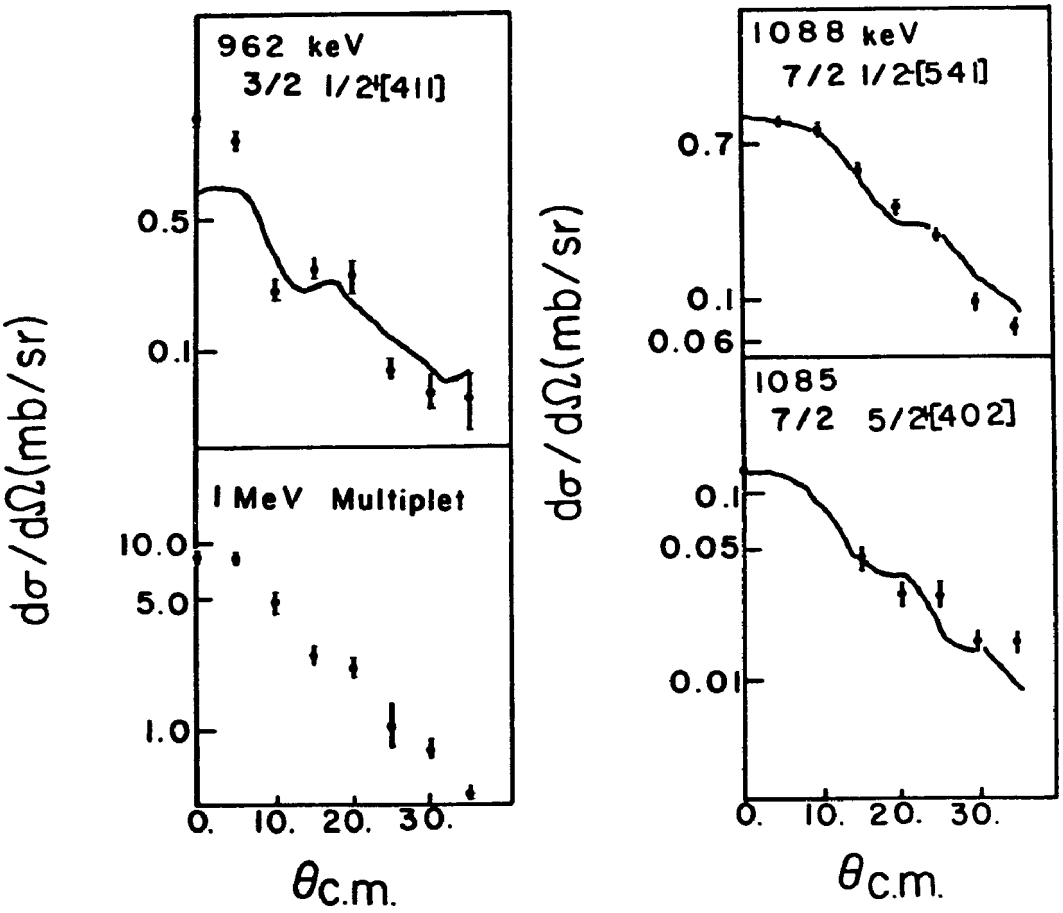


Fig. 12.--Angular distributions for the (α,t) reaction (962 to 1088 keV).

display the complementary (α,t) measurements. The error bars reflect peak-fitting, statistical, background subtraction, and plate-reading errors. The excitation energies were extracted using the energy calibration formula (G1). The a priori error calculated from the formula and the comparison of the excitation energies extracted from the two reactions indicate that the energies listed are accurate to within 15 keV. The solid lines represent distorted wave curves calculated with the parameters listed in Tables 2 and 3. The (^{3}He,d) parameters are those due to Parkinson et al.,[16] while the (α,t) parameters represent those due to Lilley and Stein,[17] as modified by Erb.[13] Neither finite range corrections nor radial cutoffs were used. All (^{3}He,d) distorted wave curves were averaged over the 4° acceptance angle of the spectrometer. The structureless nature of the (α,t) distributions made this averaging process necessary for only the $\ell = 0$ distribution. (The averaging procedure resulted in less than a 2% change in the extracted spectroscopic factor of level "2" (the 5/2 member of the ground state band) at the first subsidiary maximum, while it somewhat improved the fit of the DWBA curve to the experimental data.) Previous investigations have shown that there is considerable confusion about the proper DWBA normalization for the (α,t) reaction.[18,19] In this experiment it was found that application of the Bassel normalization factor[20] of 4.42 to the (^{3}He,d) distribution of the intense, well defined 5/2 member of the ground state

TABLE 2

OPTICAL PARAMETERS FOR THE (^{3}He,d) REACTION

Particle	V(MeV)	r_o(F)	a(F)	W(MeV)	W_D(MeV)	r_o'(F)	a'(F)	r_c(F)	V_{so}
^{3}He	175	1.14	0.723	17.5	0	1.60	0.90	1.4	0
d	91	1.16	0.83	0	14.25	1.25	0.90	1.3	0
p	V_p	1.25	0.63	---	---	---	---	1.25	(λ = 15)

TABLE 3

OPTICAL PARAMETERS FOR THE (α,t) REACTION

Particle	V(MeV)	r_o(F)	a(F)	W(MeV)	W_D(MeV)	r_o'(F)	a'(F)	r_c(F)	V_{so}
^{4}He	187	1.35	0.574	25	0	1.35	0.574	1.30	0
t	150.3	1.24	0.707	13.9	0	1.42	0.816	1.25	0
p	V_p	1.25	0.63	---	---	---	---	---	(λ = 15)

band yielded a value of $2U^2C^2/(2j+1)$ equal to 0.23. The latter parameter was then used to extract a normalization factor of ~44.2 from the complementary (α,t) distribution (accurate to within 30%). Hence, this value was set equal to the Bassel factor of 44.7. Table 4 summarizes the excitation energies, level identifications, and experimental values of U^2C^2 for ^{159}Tb. Table 5 lists the experimental values of the inertial parameter ($h^2/2\mathcal{J}_o$) and the decoupling parameter (a) for the bands observed.

It should be noted that all ℓ-transfers were identified on the basis of the characteristic shapes of the (^{3}He,d) distributions. Values of the spectroscopic strength were then deduced by comparing the experimental cross sections with the distorted wave calculations at the first maximum. After the ℓ-transfer had been ascertained, the complementary (α,t) distribution was used to obtain another estimate of the value of U^2C^2. This procedure proved to be necessary, as all (except the ℓ = 0 transfer) (α,t) distributions were structureless. In addition, the magnitudes of the (α,t) angular distributions showed a strong Q-dependence for low ℓ-transfers. It was found that a 300 keV difference in Q-value altered the value of U^2C^2 extracted from experimental data by a factor of 2.

Table 6 is a comparison of the Michigan spectroscopic data with that of Boyno[22] at Rochester and Tippett[23] at McMaster. The Rochester data were normalized to a cal-

TABLE 4

SUMMARY OF EXPERIMENTAL DATA ACQUIRED FOR ^{159}Tb

Level	Excitation energy (keV)	Signature	U^2C^2	
			(^{3}He,d)	(α,t)
1	0	3/2 3/2$^+$[411]	0.017	0.024
2	58	5/2 3/2$^+$[411]	0.68	0.68
3	131	7/2 3/2$^+$[411]		0.075
4	239	9/2 3/2$^+$[411]		0.06
5	375	5/2 5/2$^-$[532]	0.008	
6	375	5/2 5/2$^+$[413]	0.036	
7	402	7/2 5/2$^-$[532]	0.035	0.035
8	417	7/2 5/2$^+$[413]	0.37	0.54
9	442	9/2 5/2$^-$[532]	0.15	
10	539	11/2 5/2$^-$[532]	0.68	1.33[a]
11	565	1/2 1/2$^+$[411]*	0.04	
12	606	3/2 1/2$^+$[411]*	0.45	0.62
13	658	5/2 1/2$^+$[411]*	0.22	0.40[b]
14	683	7/2 1/2$^+$[411]*	0.33	
15	764	7/2 7/2$^+$[404]	0.84	1.60
16	806	11/2 7/2$^-$[523]	0.32	0.47
17	843	1/2 1/2$^-$[541]	0.10	

TABLE 4--Continued

Level	Excitation energy (keV)	Signature	U^2C^2	
			(^{3}He,d)	(α,t)
18	881	5/2 1/2$^-$[541]	0.42	0.35
19	935	1/2 1/2$^+$[411]	0.09	0.11
20	935	3/2 1/2$^-$[541]		0.02
21	962	3/2 1/2$^+$[411]	0.12	0.22
22	1005	5/2 5/2$^+$[402]	0.76	
23	1033	5/2 1/2$^+$[411]	0.54	0.37[c]
24	1068	7/2 1/2$^+$[411]	0.28	
25	1068	3/2 1/2$^-$[530][d]	0.28	
26	1088	7/2 1/2$^-$[541]	0.30	0.42
27	~ 1085	7/2 5/2$^+$[402]		0.02
28	1195	9/2 5/2$^+$[402][e]	0.40	

*Indicates lower vibrational band; upper band is indicated without asterisk.

[a]Overestimate due to overlap with the 9/2 5/2$^+$[413] and 1/2 1/2$^+$[411] levels.

[b]Overestimate due to overlap with the 7/2 1/2$^+$[411]* level.

[c]Estimate based on the assumption that the 1-MeV multiplet contains the 11/2 1/2$^-$[541] level with spectroscopic strength of 0.49.

[d]Assumed degenerate with the 1/2 1/2$^-$[530] level. Level assignment is tentative because of absence of the 3/2$^-$[532] and 9/2$^-$[514] bands.

[e]Strength attributable to a multiplet of high ℓ-transfers at 1200 keV.

TABLE 5

EXPERIMENTAL ENERGY SYSTEMATICS OF ^{159}Tb

Band	Michigan data		Bunker and Reich[21] data	
	$h^2/2\mathcal{J}_o$ (keV)	a	$h^2/2\mathcal{J}_o$ (keV)	a
$3/2^+[411]$	11.6		11.6	
$5/2^+[413]$	a		11.6	
$1/2^+[411]$*	12.	0.1	11.8	0.05
$1/2^-[541]$	9.9	2.1		
$1/2^+[411]$	b		12.	-0.81
$5/2^+[402]$	11.5			
$5/2^-[532]$	c			

[a]Bandhead was obscured by $5/2^-[532]$ bandhead.

[b]Bandhead obscured by 3/2 $1/2^-[541]$.

[c]Parameters are meaningless because of extreme Coriolis coupling.

TABLE 6

COMPARISON OF EXPERIMENTAL PROTON-STRIPPING STRENGTHS

Level	(^{3}He,d)	(α,t)	Rochester	McMaster[a]
3/2 3/2$^+$[411]	0.016	0.024	0.025	0.06
5/2 3/2$^+$[411]	0.68	0.68	0.65	0.99
7/2 3/2$^+$[411]		0.075	0.055	0.12
9/2 3/2$^+$[411]		0.06	0.16	0.08
5/2 5/2$^+$[413]	0.036			0.03
7/2 5/2$^-$[532]	0.035	0.035	0.02	0.045
7/2 5/2$^+$[413]	0.37	0.54	0.23	0.40
9/2 5/2$^-$[532]	0.15			0.10
11/2 5/2$^-$[532]	0.68	1.33	1.05	1.45
1/2 1/2$^+$[411]*	0.04		0.025	0.035
3/2 1/2$^+$[411]*	0.45	0.62	0.26	0.52
5/2 1/2$^+$[411]*	0.22	0.40	0.14	0.21
7/2 7/2$^+$[404]	0.84	1.60	0.75	1.15
11/2 7/2$^-$[523]	0.32	0.47	0.22	0.43
1/2 1/2$^-$[541]	0.10		0.045	0.09
5/2 1/2$^-$[541]	0.42	0.35	0.24	0.40
1/2 1/2$^+$[411]	0.09	0.11	0.01	0.25
3/2 1/2$^+$[411]	0.12	0.22	0.085	0.25
5/2 5/2$^+$[402]	0.76		0.95	1.0
5/2 1/2$^+$[411]	0.54	0.37	0.07	
7/2 1/2$^+$[411]	0.28		0.05	
7/2 1/2$^-$[541]	0.30	0.42		0.03

[a]Assumed to be one-half the sum of the experimental values of U^2C^2.

culated value of the spectroscopic strength of the 5/2 member of the ground state band by means of a renormalization factor, which increased the Bassel normalization factors by 100%. Hence, the Rochester data are expected to be a factor of 2 smaller than the Michigan and the McMaster data. Beyond 850 keV excitation, the assignments of Boyno and of Tippett are considered tentative. In addition, neither set of data describes the $7/2^+$ state at 688 keV.

B. Calculation of Coriolis Mixed Spectroscopic Strengths

The matrix elements involved in Coriolis coupling calculations have been discussed in Chapter I. It was noted that they depend on the Nilsson coefficients $c_{j\Omega}$, the pairing parameters U and V, and the single-particle energies. The inelastic scattering measurements of Hendrie et al.[24] indicate that the quadrupole deformation of ^{158}Gd is approximately 0.27. Hence, the Nilsson tables of Chi[25] for $\kappa = 0.0500$ and $\mu = 0.630$ were interpolated to yield the pertinent coefficients. An article by Marshalek,[26] which listed a best fit to the solutions of the pairing equations in the rare-earth region, implied that the pairing gap parameter Δ for ^{158}Gd was ~800 keV. Rudimentary Coriolis calculations showed that the 3/2 member of the ground state band was only weakly affected by Coriolis mixing. Hence, the experimental spectroscopic strength of this level was used to deduce the location of the Fermi

level at ~-248 keV with respect to the $3/2^+[411]$ Nilsson ground state. The single-particle energies used in the evaluation of the pairing parameters were assumed to be given by the Nilsson eigenenergies. The single-particle energies used in the Coriolis matrix were assumed to be given by the quasiparticle energy difference:

$$\sqrt{(E_{exc}-\lambda)^2+\Delta^2} - \sqrt{(E_{G.S.}-\lambda)^2+\Delta^2}$$

where the E's represent the Nilsson single particle energies. Since this difference is not well known experimentally, it was allowed to vary within ±100 keV of its calculated value. In most cases the coupling was found to be so weak that the difference in quasiparticle energies could be approximated by the experimental excitation energy. No attempts were made to incorporate demagnification parameters,[27] as this process would only increase the number of adjustable parameters in the calculation.

The odd-parity mixing calculations were carried out by incorporating the $1/2^-[541]$, $1/2^-[550]$, $3/2^-[541]$, $3/2^-[521]$, $3/2^-[532]$, $5/2^-[523]$, $5/2^-[532]$, $7/2^-[523]$, $9/2^-[514]$, $11/2^-[505]$, and $1/2^-[530]$ bands in the Coriolis coupling matrix. A trial calculation involving only the $5/2^-[532]$ and $7/2^-[523]$ bands showed that the latter were the most strongly affected by Coriolis mixing. A comparison of the experimental and calculated spectroscopic strengths is given in Table 7.

TABLE 7

COMPARISON OF THE EXPERIMENTAL AND THEORETICAL SPECTROSCOPIC STRENGTHS (U^2C^2) FOR THE ODD-PARITY STATES

Level	Experiment	Theory
5/2 5/2⁻[532]	0.008	0.001[a]
7/2 5/2⁻[532]	0.035	0.023
9/2 5/2⁻[532]	0.15	0.065
11/2 5/2⁻[532]	0.68	0.80
11/2 7/2⁻[523]	0.47′	0.520
1/2 1/2⁻[541]	0.10	0.044
5/2 1/2⁻[541]	0.35	0.27
3/2 1/2⁻[541]	0.03′	0.048
7/2 1/2⁻[541]	0.29	0.062
3/2 1/2⁻[530]	0.28	0.28[b]

′Denotes (α,t) data.

[a]Not Coriolis mixed.

[b]Not Coriolis mixed, includes a small correction for 1/2-3/2 degeneracy. Assignment tentative.

The even-parity states were restricted to the $3/2^+[411]$, $5/2^+[413]$, $1/2^+[411]$, $5/2^+[402]$, and $7/2^+[404]$ bands. The basis was thus limited because preliminary calculations indicated that the splitting of the $1/2^+[411]$ band into two fragments by vibrational mechanisms would account for the majority of the uncertainties in the calculations. Various proportions of the $1/2^+[411]$ single-particle strength were incorporated into the coupling matrices involving the bands originating at 580 and 935 keV. The best agreement with experimental data was found when the band was fragmented in a 2:1 ratio--either with 67% in the lower band and 33% in the upper band or vice versa. Hence, two sets of spectroscopic strengths are compared with experimental data in Table 8. It is clear that neither configuration successfully accounts for the spectroscopic strength of every level. However, both configurations predict reasonable strengths for the bands unaffected by vibrational mixing. This is physically plausible, since the bands with vibrational content exhibit a small energy separation (~350 keV), while the only band with which they can directly couple, i.e., the $3/2^+[411]$ ground state band, is ~600 keV distant. The use of Nilsson coefficients corrected for hexadecapole deformation showed no distinct improvement when Coriolis mixing was considered. The 5-10% variation in Nilsson coefficients was completely obscured by Coriolis coupling.

TABLE 8

COMPARISON OF THE EXPERIMENTAL AND THEORETICAL SPECTROSCOPIC STRENGTHS (U^2C^2) FOR THE EVEN-PARITY STATES

Level	Experiment	67% $1/2^+[411]$ at 935 keV	33% $1/2^+[411]$ at 935 keV
3/2 $3/2^+[411]$	0.016	0.019	0.018
5/2 $3/2^+[411]$	0.68	0.56	0.57
7/2 $3/2^+[411]$	0.075′	0.154	0.153
9/2 $3/2^+[411]$	0.06′	0.04	0.04
5/2 $5/2^+[413]$	0.036	0.034	0.034
7/2 $5/2^+[413]$	0.37	0.45	0.45
1/2 $1/2^+[411]$*	0.04	0.076	0.052
3/2 $1/2^+[411]$*	0.45	0.18	0.34
5/2 $1/2^+[411]$*	0.22	0.041	0.089
7/2 $1/2^+[411]$*	0.33	0.069	0.13
7/2 $7/2^+[404]$	0.84	0.81	0.81
1/2 $1/2^+[411]$	0.09	0.055	0.028
3/2 $1/2^+[411]$	0.22	0.31	0.15
5/2 $1/2^+[411]$	0.54	0.12	0.065
7/2 $1/2^+[411]$	0.28	0.13	0.052
5/2 $5/2^+[402]$	0.76	0.83	0.83
7/2 $5/2^+[402]$	0.02′	0.11	0.05
9/2 $5/2^+[402]$	0.40[a]	0.017	0.017

′Denotes (α,t) data.

[a]Strength attributable to a multiplet of high ℓ-transfers at 1200 keV.

C. Discussion

As Tables 7 and 8 imply, members of the $3/2^+[411]$, $5/2^+[413]$, $5/2^-[532]$, $7/2^-[523]$, $5/2^+[402]$, $7/2^+[404]$, $1/2^-[541]$, and $1/2^-[530]$ bands were observed as well as elements of the two vibrationally-mixed $1/2^+[411]$ fragments. A brief discussion of the theoretical and experimental peculiarities of these bands is given below.

Even-parity bands

$3/2^+[411]$.--The members of the ground state band have been exhaustively studied in Coulomb excitation and decay studies.[28,29] All members of the $3/2^+[411]$ band are visible in the (α,t) spectra. In the 25°-30° region, however, the 9/2 member had to be disentangled from a ^{160}Gd impurity nearby. The 7/2 and 9/2 members of this band are so weakly excited in the $(^3He,d)$ experiment that their location in the spectrum must be considered tentative; this observation is reasonable because of the tendency of the $(^3He,d)$ reaction to preferentially populate low ℓ-transfer levels. Since the decay studies enabled one to deduce the ℓ-transfers of the 7/2 and 9/2 states, the (α,t) distributions were used to extract the spectroscopic strengths. (The overestimate in the reaction cross sections at 15° was traced to plate-reading errors and was not used.) Although Table 8 shows that the experimental values of U^2C^2 agree reasonably well with those predicted by Coriolis

mixing calculations, it is clear that Coriolis mixing gives too much enhancement to the 7/2 member. The ratio of the experimental strengths, 0.03:1:0.12:0.09, shows better agreement with the theoretical ratio predicted by the Nilsson model without Coriolis mixing, 0.04:1:0.16:0.04. Insertion of the hexadecapole correction produced little improvement, since it yielded a value of $U^2C^2 \approx 0.035$, which proved to be insensitive to variation of all parameters. (A hexadecapole deformation of 0.05 was used, following the work of Hendrie et al.[24]) The experimental value of the inertial parameter, $h^2/2\mathcal{J}^o$ = 11.6 keV, is in agreement with that observed in decay work.

$5/2^+[413]$.--The 7/2 member of this band, predicted to contain most of the strength of this $g_{7/2}$-originating band, was clearly observed in both reactions at 417 keV with a spectroscopic strength of ~0.35. The 5/2 member was deduced by indirect means. Hill and Wiedenbeck[29] show that this level was 15 keV distant from the bandhead of the $5/2^-[532]$ band. A broad level was observed in the (^{3}He,d) distributions with a centroid at ~373 keV excitation. It was found that the composite level could be decomposed (approximately) into $\ell = 2$ and $\ell = 3$ components. Because of the poor statistics and the errors inherent in the decomposition procedure, no better than 40% accuracy can be ascribed to the results. Table 8 shows that, never-

theless, the predicted spectroscopic strengths for the 5/2 and 7/2 members of this band are in reasonable agreement with the experiment. The 9/2 member is predicted to lie at 560 keV with a value of $U^2C^2 = 0.068$ (assuming an inertial parameter of 11.6 keV). Hence, this member is expected to lie very close to the $11/2^-$ state at 530 keV. This may account for the unreasonably large spectroscopic strength attributed to the $11/2^-$ state in the (α,t) measurements.

$5/2^+[402]$.--The mixing calculations predict that the 5/2 member of this band should be the strongest state in the spectrum with a spectroscopic strength of ~0.83. This state appears to be the lowest lying member of the multiplet with a centroid at ~1 MeV. The level shows a clearcut $\ell = 2$ character and yields a value of $U^2C^2 = 0.76$. In the few cases in which the 1-MeV multiplet was accurately resolved in the (α,t) study, the same (within experimental error) spectroscopic strength was deduced. Under the assumption that the inertial parameter was 11.5 keV, it was possible to identify the $7/2^+$ state at ~1085 keV in the (α,t) distribution with the 7/2 member of this band. (The experimental value of $U^2C^2 = 0.02$ agrees favorably with the value of 0.05 predicted by the Coriolis calculations.) In addition, the (^{3}He,d) experiment inferred the presence of an $\ell = 4$ transition at 1195 keV,

the predicted location of the 9/2 member of this band. The (α,t) distributions showed that this level is a multiplet of high-ℓ states. Hence, the inordinately large spectroscopic strength of this state (0.40) deduced from the (^{3}He,d) distribution is probably attributable to a mixture of high-states. Hence, the ℓ = 4 transition at 1195 keV may be only tentatively assigned as the 9/2 member of this band.

$7/2^+[404]$.--Since this band derives its origin from the $g_{7/2}$ shell model state, most of the strength of this band is predicted to be concentrated in the 7/2 member. In both reactions an intense ℓ = 4 transition was observed at 764 keV with experimental strengths of 0.84 and 1.59 in the (^{3}He,d) and (α,t) reactions, respectively. The calculated strength is 0.813. The overestimate of the (α,t) strength is probably a Q-value effect. The 9/2 member of this band should be located at 870 keV and is predicted to be very weak. The state is not observed in either reaction.

(γ, $3/2^+[411]$), $1/2^+[411]$.--The members of the K = 1/2 band of Diamond et al.[28] have been observed at 565, 606, and 658 keV with an additional member at 683 keV. The latter was obscured in the (α,t) study because of overlap with the 606 keV state. In addition, the weakly excited transition at 565 keV was obscured by the tail of the $11/2^-$ state at 530 keV in the (α,t) reaction. The

levels appear to be the 1/2, 3/2, 5/2, and 7/2 members of a rotational band. The experimental strengths are in the ratio 1:11:6:8. If one neglects the strength of the 1/2 member of the band because of the lack of strength, the last three members yield the strength ratio 11:6:8. The theoretical strength ratio for the 3/2, 5/2, and 7/2 members of a pure $1/2^+[411]$ band is predicted to be 6:2:2. Hence, the band appears to be a fragment of the $1/2^+[411]$ band, as predicted by Soloviev.[6] Table 8 has shown that no reasonable estimate of the $1/2^+[411]$ single-particle admixture in this state can account for the large experimental strengths of the 5/2 and 7/2 members of this band. The nature of the reaction mechanism appears to be important for a detailed description of the nuclear character of this state because of vibrational admixtures. In short, transitions to these levels appear to proceed via multistep processes, such as target excitation and subsequent stripping. In addition, the 7/2 member of this band appears to lie 80 keV below the predicted location. It is unlikely that Coriolis mixing can account for such a drastic energy distortion.

At 935, 962, and 1033 keV, the 1/2, 3/2, and 5/2 members of a similar band appear. This band has been traditionally considered to be the $1/2^+[411]$ band with $\hbar^2/2\mathcal{I}_0$ = 12 keV and a =-0.81.[21] These parameters, having been validated for the three clearly visible members of the

band, were used to estimate the position of the 7/2 member of this band. With this calculation as a guide, it was deduced that the 1068 keV level could be described as a doublet containing $\ell = 1$ and $\ell = 4$ components. The $\ell = 1$ component will be discussed in a later section. The $\ell = 4$ component yielded a value of $U^2C^2 = 0.28$ for the 7/2 member of this band.

The 5/2 member of this $1/2^+[411]$ band lies in the multiplet at 1 MeV. The long tails on the (α,t) peaks as well as the inadequate resolution in that reaction made accurate disentanglement of the 1-MeV multiplet impossible. However, exhaustive study of the well resolved (^{3}He,d) data revealed that the 9/2 member of the $1/2^-[541]$ band, which was predicted to lie in the 1-MeV vicinity with a spectroscopic strength of ~0.49, could not be disentangled from the spectra because of the many low ℓ-transfers at 1 MeV. Hence, the entire experimental multiplet from the (α,t) reaction was compared with the contributions from each of its component levels, including the predicted contribution of the 9/2 member of the $1/2^-[541]$ band. Since the mixing calculations predicted that the latter state should be nearly degenerate with the 5/2 member of the upper $1/2^+[411]$ fragment, the composite calculation was used to estimate the error in the spectroscopic strength of this state because of neglect of the 9/2 member of the $1/2^-[541]$ band. The calculations showed that this could lead to an overes-

timate of the strength of the $5/2^+$ state of no greater than 25%.

The final conclusion of the analysis is, therefore, that the Coriolis predictions for the 5/2 and 7/2 members of this band are far too small. Considerable enhancement is required to account for the experimentally observed strengths. It is interesting to note that Soloviev[6] predicts this level to be entirely vibrational. The strongly vibrational character of the band indicates that it is likely that the scattering amplitude contains nonnegligible components due to inelastic excitation to the γ-vibrational level in ^{158}Gd and subsequent stripping as well as stripping and subsequent inelastic de-excitation. In short, multistep mechanisms appear to be important. This effect may account for the discrepancy between the experimental strength ratio (1:1.3:6:1.6) and the predicted strength ratio for the $1/2^+[411]$ band (1:6:2:2).

On the basis of energy systematics, the experimental decoupling parameter of the lower band (+0.05) seems to indicate that the state is largely vibrational, while the decoupling parameter of the higher band (-0.81) implies a single-particle character. If this were the case, the lower band would be populated weakly (or not at all) in particle-transfer reactions. The data clearly contradict this thesis. The lower band shows appreciable strength, while the higher band shows a grossly distorted finger-

print. The calculations of Bunker and Reich[21] also contradict the assumption that the upper band is primarily of a single-particle nature. In conclusion, the results of the present analysis indicate that neither band is purely single-particle. They both contain vibrational admixtures, which can be legitimately studied solely by a detailed treatment of the complex reaction mechanisms involved.

Odd-parity bands

$5/2^-[532]$ and $7/2^-[523]$.--The $5/2^-[532]$ hole state ($U^2 \approx 0.16$) and the $7/2^-[523]$ particle state ($U^2 \approx 0.83$) exhibit a ΔK of unity and a predicted quasiparticle energy separation of no greater than 250 keV. Hence, they are expected to exhibit strong Coriolis mixing, which renders attempts to attribute standard single-Nilsson orbital parentage to the levels observed meaningless. Because of the strong coupling, the definition of a single inertial parameter becomes hopeless.

As the discussion of the $5/2^+[413]$ band infers, the proximity of the $5/2^-$ state to the $5/2^+[413]$ bandhead has rendered analysis of the former as a single, clearcut level impossible. The poor statistics and the inaccuracy of the method used to disentangle closely-spaced doublets infer the tentative nature of the value of U^2C^2 derived (0.008). The mixing calculations predict a value of 0.000, while the uncoupled value is ~0.001. This infers that the

Coriolis matrix elements are probably too strong and, hence, require a demagnification factor.

The $7/2^-$ level at 402 keV was clearly observed in both reactions and yielded an experimental spectroscopic strength of ~0.035. The calculated value of 0.023 appears reasonable in view of the uncertainty involved in extracting spectroscopic data for weakly-excited states.

The (^{3}He,d) data yielded an $\ell = 5$ transition at 442 keV, with extremely poor statistics. In much of the (α,t) data, the level was obscured by the long tail of the 7/2 member of the $5/2^+[413]$ band. When observed, the (α,t) peak yielded spectroscopic strengths within 10% of that crudely obtained from the (^{3}He,d) data. The value of $U^2C^2 = 0.15$ is a factor of 2 larger than the Coriolis prediction. Nevertheless, the assignment may be made because the lack of accuracy in peak-fitting for a weakly-excited level may account for the large discrepancy between theory and experiment.

The mixing calculations predict no other 5/2, 7/2, or 9/2 levels of appreciable intensity in the 300-500 keV excitation range and none has been observed.

Two strong $\ell = 5$ states appear at 539 and 806 keV in both reactions. It has been mentioned in the discussion of the $5/2^+[413]$ band that the experimental spectroscopic strength of the lower level has been overestimated in the (α,t) experiment because of interference from the 9/2 member of the

$5/2^+[413]$ band. The experimental spectroscopic strengths of 0.68 and 0.47 are in reasonable agreement with the calculated values of 0.80 and 0.52.

$1/2^-[541]$.--The levels at 843, 881, and 1088 keV with respective ℓ-transfers of 1, 3, and 3 appear to be the 1/2, 5/2, and 7/2 members of the $1/2^-[541]$ band with inertial parameter $\hbar^2/2\mathcal{J}_0 = 10$ keV and decoupling parameter $a = 2.1$. The level at 843 keV was visible only at forward angles in the (α,t) experiment because of obfuscation by the long tail of the $11/2^-$ state at 806 keV. The $1/2^-$ member appears to be the $1/2^-$ state observed at 860 keV in the decay work of Hill and Wiedenbeck.[29] The 3/2 member was predicted to lie at 935 keV, while the 9/2 member was predicted to form a doublet with the 5/2 member of the upper vibrational state. The latter, although unobserved, was used to estimate the error in the 5/2 member of the upper vibrational band (as the discussion of that band has indicated), while the former could be inferred to be accurate provided that one added a small $\ell = 1$ component to the $\ell = 0$ transition at 935 keV in the (α,t) work (implying that the level is, in fact, a doublet). Application of this procedure to the corresponding (^{3}He,d) distribution would appear fruitless because of the peak-fitting process in that analysis which neglected the presence of the Landau tails on the peaks. Needless to say, the uncertainty in

the spectroscopic strength quoted for the 3/2 member is large. The $11/2^-$ state, predicted to lie at ~1300 keV, falls out of the range of this experiment. The Coriolis calculations, displayed in Table 7, predict strengths that are a factor of 2 smaller than the experimental values. A similar effect has been observed in the holmium studies performed at this laboratory,[30] which demonstrated the remarkable fragmentation of the band and the poor fit of the data to predicted angular distributions. A tentative explanation implies that the irregularities may be attributed to the presence of a gamma-vibrational band based on the $5/2^-[532]$ band, which would be expected to mix with the $1/2^-[541]$ band. However, the absence of any vibrational bands at these excitation energies in the spectra of Diamond et al.[28] appears to rule out this explanation. The holmium studies also indicated that the introduction of sophisticated multistep reaction mechanisms failed to account for all of the observed spectroscopic strengths.

$1/2^-[530]$.--The $\ell = 1$ transition at 1068 keV, if assumed to be a $3/2^-$ level, yields an experimental spectroscopic strength of $U^2C^2 = 0.28$. The Nilsson model predicts that the next three odd-parity bands to be occupied are the $9/2^-[514]$, $3/2^-[532]$, and $1/2^-[530]$ bands. No evidence for the presence of the $9/2^-[514]$ band has been found. However, the bulk of the strength of this band is

predicted to lie in the 11/2 member. Hence, it is possible that this strong $\ell = 5$ transition lies outside the 1200 keV range of this study. The Nilsson model predicts that the value of C^2 for the 3/2 member of the 3/2⁻[532] band ≤ 0.01. Hence, the value of U^2C^2 for this level ≤ 0.01. It is highly unlikely that Coriolis mixing can produce the 28-fold increase necessary to make this parameter agree with the experimental strength of 0.28. The 1/2⁻[530] bandhead is predicted to lie ~300 keV above the 3/2⁻[532] bandhead. The decoupling parameter of -1.6 implies near-degeneracy between the 1/2 and 3/2 members of this band. The non-Coriolis mixed value of U^2C^2 for the 3/2 member is predicted to be ~0.25. Addition of a small enhancement predicted by the degeneracy yields a value of $U^2C^2 = 0.28$. Coriolis calculations predicted strong mixing between the 1/2⁻[541] and 1/2⁻[530] bands, which resulted in unrealistically small strengths for the members of the 1/2⁻[541] band. Although the level density at 1300 keV is rather high in the (α,t) spectrum, a level, which showed an approximately correct magnitude for the 11/2 member of the 1/2⁻[530] band, was located in this vicinity. (As a guide in locating the level, it was assumed that $h^2/2\mathfrak{I}_o \approx 10$ keV and $a \approx -1.6$.) Nevertheless, the absence of the 9/2⁻[514] and 3/2⁻[532] bands renders the assignment of the 1068-keV $\ell = 1$ transition as the bandhead of the 1/2⁻[530] band extremely tentative.

CONCLUSIONS

The $^{158}Gd(\alpha,t)^{159}Tb$ and $^{158}Gd(^{3}He,d)^{159}Tb$ studies described in this dissertation allow one to identify with confidence the presence of the $3/2^{+}[411]$, $5/2^{+}[413]$, $5/2^{-}[532]$, $7/2^{-}[523]$, $5/2^{+}[402]$, $7/2^{+}[404]$, and $1/2^{-}[541]$ single-particle bands as well as the two vibrational bands with $1/2^{+}[411]$ single-particle components. The (^{3}He,d) reaction proved to be of great value in identifying the angular momenta of the states because of its shape dependence on ℓ-transfer. In addition, the well known Bassel normalization factor of 4.42 made extraction of spectroscopic information consistent and reliable. On the other hand, the (α,t) distribution, with its strong Q-dependence and lack of structure, provides no more than a check on the (^{3}He,d) work. At the high bombarding energies utilized the combination of structure in the (^{3}He,d) reaction (which often deviates from DWBA predictions) and Q-dependence in the (α,t) reaction renders spectroscopic studies by means of cross sectional ratios highly unreliable. This is particularly true in the analysis of doublets of levels emanating from different ℓ-transfers. At lower bombarding energies, where both reactions display little structure, the cross sectional ratios may be more meaningful.

The standard one-step direct reaction mechanism appears to account for the spectroscopic information deduced for most of the levels populated, provided that one assumes that Coriolis mixing accounts for the spectroscopic strengths of the states. Analysis of vibrationally-mixed levels by one-step processes fails to account for the magnitude of the cross sections. Hence, further analytical study of these levels involving more complex reaction processes is required before a complete understanding of their nuclear structure can be attained.

REFERENCES

1. Third Baron Rayleigh, The Theory of Sound, Vol. II (Macmillan, 1977).

2. M. A. Preston, Physics of the Nucleus (Addison-Wesley, 1962).

3. L. D. Landau and E. M. Lifschitz, Quantum Mechanics (Non-Relativistic Theory) (Addison-Wesley, 1959).

4. S. G. Nilsson, K. Danske Vidensk. Selsk. Mat.--Fys. Medd; 29, No. 16 (1955).

5. Bent Elbek and Per Olav Tjøm, Annual Reviews of Nuclear Science, 259 (1969).

6. V. G. Soloviev and P. Vogel, Nuclear Physics, A92, 449 (1967).

7. G. R. Satchler, in Lectures in Theoretical Physics, Vol. VIII (University of Colorado Press, 1966).

8. L. W. Borgman, University of Michigan, thesis (unpublished).

9. W. C. Parkinson and J. Bardwick, Nucl. Inst. and Methods, 78, 245 (1970).

10. Yissum Research Development Company, Jerusalem, Israel.

11. W. C. Parkinson in a series of lectures at the University of Michigan Cyclotron Laboratory.

12. A. S. Broad, University of Michigan (private communication).

13. K. A. Erb, University of Michigan, thesis (unpublished).

14. J. R. Comfort, Argonne National Laboratory (unpublished).

15. A. S. Broad and D. A. Lewis, University of Michigan (private communication).

16. W. C. Parkinson, D. L. Hendrie, H. H. Duhm, J. Mahoney, J. Saudinos, and G. R. Satchler, Phys. Rev., 178, 1976 (1969).

17. J. S. Lilley and Nelson Stein, Phys. Rev. Letters, 19, 709 (1967).

18. R. H. Price, D. G. Burke, and M. W. John, Nuclear Physics, A176, 354 (1971).

19. M. T. Lu and W. P. Alford, Phys. Rev., C3, 1243 (1971).

20. R. H. Bassel, Phys. Rev., 149, 791 (1966).

21. M. E. Bunker and C. W. Reich, Reviews of Modern Physics, 43, 348 (1971).

22. J. S. Boyno and J. R. Huizenga, Phys. Rev., C6, 1411 (1972).

23. J. S. Tippett, McMaster University, thesis (unpublished).

24. D. L. Hendrie, N. K. Glendenning, B. G. Harvey, O. N. Jarvis, H. H. Duhm, J. Saudinos, and J. Mahoney, Physcis Letters, 26B, 127 (1968).

25. B. E. Chi, Nuclear Physics, 83, 97 (1966).

26. E. R. Marshalek, Phys. Rev., 158, 993 (1967).

27. G. Winter, L. Funke, K. H. Kaun, P. Kemnitz, and H. Sodan, Nuclear Physics, A176, 609 (1971).

28. R. M. Diamond, B. Elbek, and F. S. Stephens, Nuclear Physics, 43, 560 (1963).

29. J. C. Hill and M. L. Wiedenbeck, Nuclear Physics, A111, 457 (1968).

30. A. S. Broad, University of Michigan, thesis (unpublished).